

Multi-omic Spatial Analysis Reveals Targetable Macrophage-Mediated Mechanisms of Immune Evasion in Hepatocellular Carcinoma Minimal Residual Disease

Lea Lemaitre^{1*}, Nia Adeniji^{1*}, Akanksha Suresh^{1*}, Reshma Reguram¹, Josephine Zhang¹, Jangho Park¹, Amit Reddy¹, Alejandro E. Trevino², Aaron T. Mayer², Anja Deutzmann³, Aida Hansen⁴, Ling Tong³, Vinodhini Arjunan¹, Neeraja Kambham⁵, Brendan Visser⁶, Monica Dua⁶, Andrew Bonham⁶, Nishita Kothary⁷, H. Blaize D'Angio², Ryan Preska², Yanay Rosen⁸, James Zou⁸, Vivek Charu⁵, Dean W. Felsher^{3#} and Renumathy Dhanasekaran^{1#}

1. Division of Gastroenterology and Hepatology, Stanford University, CA
2. Enable Medicine, CA 94025, USA
3. Division of Oncology, Departments of Medicine and Pathology, Stanford University, CA
4. Department of Biomedicine, Aarhus University, Aarhus C 8000, Denmark
5. Department of Pathology, Stanford University, CA
6. Department of Surgery, Stanford University, CA
7. Department of Radiology, Stanford University, CA
8. Department of Biomedical Data Science and Computer Science, Stanford, CA 94305.

Potential conflicts of interest- A.T.M., A.E.T., R.P., and H.B.D are employees of Enable Medicine.
No other conflicts of interest

Running Title: Targeting Macrophage-mediated Mechanisms of HCC Recurrence

Keywords: Residual, MRD, Macrophage, exhausted T cell, TGFB

*Co-First Authors

#Co-Corresponding Authors

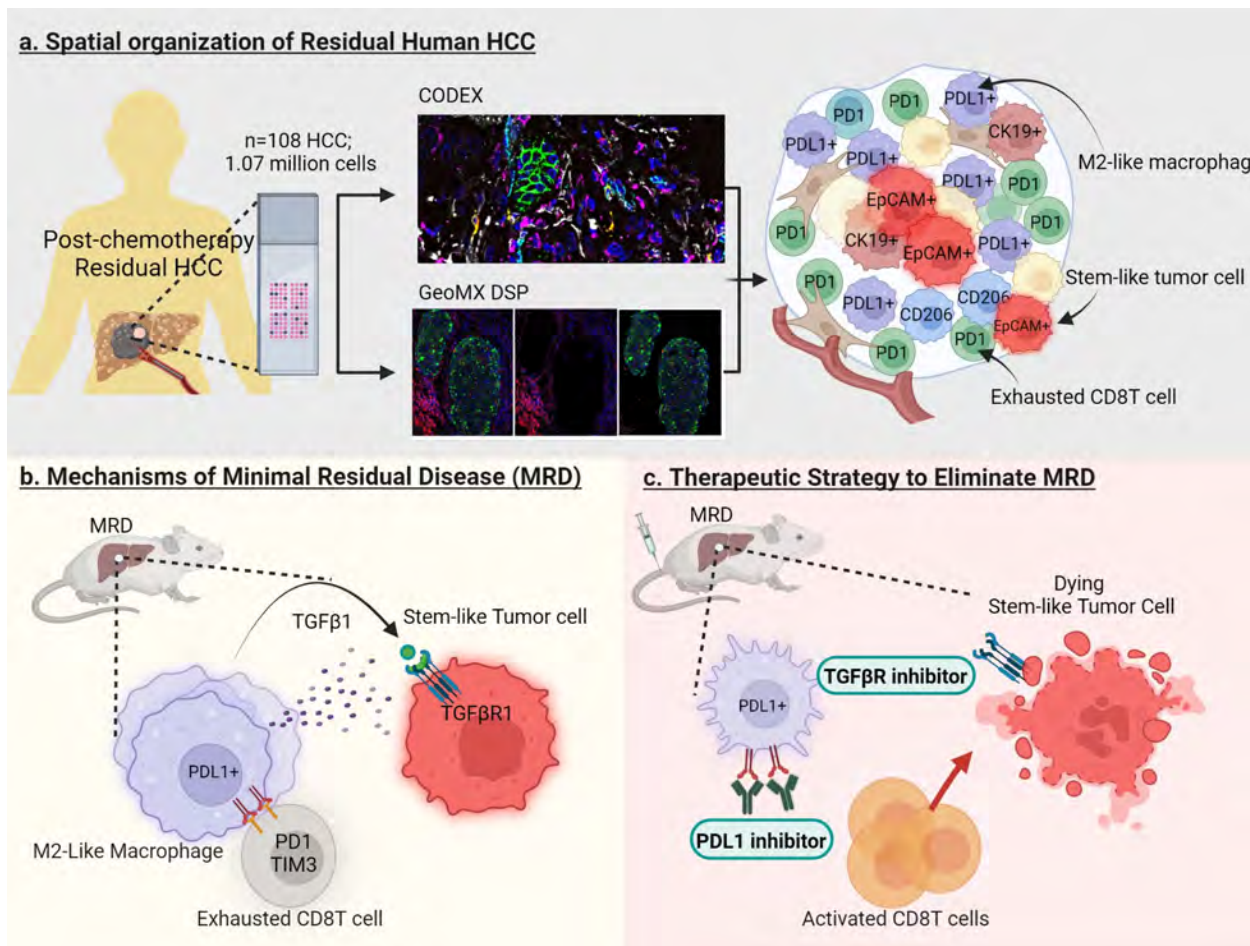
Address correspondence to:

Renumathy Dhanasekaran MD PhD
Assistant Professor
Division of Gastroenterology and Hepatology
Department of Medicine
300 Pasteur Drive, Alway Building M209
Stanford University, Stanford, CA, 9430
Email: dhanaser@stanford.edu

Or

Dean W. Felsher MD PhD
Professor
Department of Medicine-Oncology and Pathology
269 Campus Drive, CCSR 1121
Stanford, CA, 94304
Email: dfelsher@stanford.edu
Telephone: 650-725-6454; Fax: (650) 725-1420

Graphical Abstract



a. The spatial organization of residual HCC is unveiled through integrated analysis of single-cell spatial profiling employing CODEX and GeoMx spatial transcriptomics of human HCC. b. TGF β 1 derived from PDL1+ macrophages enable the persistence of residual stem-like tumor cells and induces the exhaustion in CD8T cells. c. In a transgenic mouse model of minimal residual disease (MRD) we target the TGF β pathway and PDL1, eliminating residual tumor cells and preventing HCC recurrence.

ABSTRACT

Hepatocellular carcinoma (HCC) frequently recurs even after initial complete response to therapy, due to the persistence of minimal residual disease (MRD). Here, we identified the mechanisms of persistence of residual tumor cells through single-cell spatial transcriptomic and proteomic analyses of both post-chemoembolization residual human HCC and transgenic mouse models of MRD. We defined the spatial organization of residual human HCC into neighborhoods within which EpCAM+/CK19+ stem-like tumor cells interact with PDL1+ M2-like macrophages. This was associated with PD1+/TIM3+ CD8T cell exhaustion and poor recurrence-free survival. Then, through spatially resolved transcriptomic analysis, we identified macrophage-mediated TGF β 1 pathway activation as a mediator of persistence of residual tumor cells. Through a mouse model of MRD, we demonstrated that Tgf β r1+ residual stem-like tumor cells survive in Tgf β 1+/Pdl1+ macrophage-rich niches which enforce CD8T cell exhaustion and enable tumor recurrence. Finally, in two mouse models: a transgenic mouse model of MRD and a syngeneic orthotopic allograft model of doxorubicin-resistant HCC, we found that the combined blockade of Tgf β and Pdl1 pathways excluded immunosuppressive macrophages, thereby recruiting activated CD8T cells that eliminate residual tumor cells. Thus, through spatial mapping, we have identified the mechanistic roles of the TGF β and PDL1 pathways in persistence of residual tumor cells in human HCC. Targeting these pathways holds therapeutic potential to eliminate MRD, which could reduce recurrence and improve patient outcomes.

INTRODUCTION

Hepatocellular carcinoma (HCC) is associated with high rates of recurrence which contribute to a grim 5-year survival rate below 20%¹. In patients with nonmetastatic HCC who respond well to transarterial chemoembolization (TACE), most but not all tumor cells are eliminated, leaving behind a small fraction of residual tumor cells. Even after prolonged latency, these residual tumor cells can lead to recurrence, which is generally unresponsive to therapy and contributes to poor survival^{2–5}. Consequently, uncovering the mechanisms that enable post-therapy residual tumor cells to persist and evade immune surveillance is pivotal to preventing recurrence and improving outcomes.

Residual tumor cells may employ two major mechanisms to persist after therapy, tumor cell intrinsic mechanism or host immune based mechanism. First, a subset of residual cells could function as stem-like tumor cells, characterized by their unique attributes such as chemoresistance and a propensity to instigate tumor recurrence^{6–10}. This perspective, despite ongoing debates, is increasingly gaining consensus^{11,12}. Previously, we have reported a transgenic mouse model of HCC tumor dormancy with such persistence of residual tumor cells with stem cell-like features¹³. Second, pro-tumor macrophages, which are dominant immune cells in HCC, can also promote recurrence^{14–16}. This is also supported by our observation of an M2-like macrophage population enabling host immune cell evasion¹⁷ and metastasis¹⁸ in mouse models of HCC. While both tumor-intrinsic and immune mechanisms can contribute to HCC recurrence, how they interact and depend on each other is unclear.

We aimed to evaluate the interplay between tumor cell-intrinsic and host immune mechanisms contributing to the persistence of residual tumor cells. To do this, we analyzed both human clinical specimens as well as multiple mouse models of HCC. First, we examined human clinical samples of residual HCC which persisted after transarterial chemoembolization (TACE). Using

single-cell spatial transcriptomic and proteomic analyses¹⁹⁻²¹, we created a spatial map of tumor-immune interactions in post-TACE residual human HCC. We identified interactions between stem-like tumor cells and pro-tumor macrophages, showed this was associated with CD8T cell exhaustion and identified a role for macrophage-mediated TGFβ pathway activation. Second, we employed three distinct yet complementary mouse models: two immunocompetent transgenic models mimicking minimal residual disease (MRD) and a syngeneic orthotopic allograft model mimicking chemoresistance. In our transgenic mouse models of non-metastatic (TRE-MYC-Cebpb-tTA¹³) and metastatic HCC (TRE-MYC/Twist1/Luc-Cebpb-tTA¹⁸), oncogene inactivation led to tumor regression, but radiologically-undetectable MRD persisted, and gave rise to recurrent tumors upon oncogene re-activation. We also developed a syngeneic orthotopic allograft model of HCC resistant to doxorubicin, the most common chemotherapeutic agent used in TACE. In both mouse models targeting the TGFβ and PDL1 pathways eliminated residual tumor cells and prevented recurrence.

RESULTS

High dimensional single-cell spatial atlas reveals tumor and immune heterogeneity in human HCC

To elucidate the spatial organization of tumor and immune cells in post chemoembolization residual HCC, we constructed a comprehensive single-cell spatial map of human HCC. We microdissected areas of viable HCC, constructed formalin-fixed paraffin-embedded (FFPE) tissue microarrays (TMA), and used co-detection by indexing (CODEX) to analyze the spatial architecture. We imaged a total of 1.07 million cells from 108 HCC samples with multiplex staining using 41 antibodies targeting tumor, immune, stromal, and functional markers (Fig 1a, Supp Fig 1, Supp Table 1). Through cellular segmentation, marker quantification, normalization, and unsupervised clustering, we identified 11 major cell types within HCC (Fig 1b, Supp Fig 2a). Thus, by utilizing FFPE-optimized CODEX, we achieved highly multiplexed single-cell marker visualization and cellular phenotyping in human HCC.

We used canonical marker expression in CODEX to further subset three major cell types: tumor cells, macrophages and T cells (Fig 1c-d). First, among the tumor cells we identified three discrete subsets. Two were stem cell-like, CK19+ (6.7%, 34436 cells) and EpCAM+ (5.2%, 26622 cells) tumor cells (Fig. 1c-d). They expressed stemness, pro-survival and mesenchymal markers (Supp Fig 2b). A third subset of tumor cells expressed the immune checkpoint PDL1 (3.8%, 19737 cells). The heterogeneity observed among these tumor cell subsets aligned with prior reports from single marker studies²²⁻²⁴. Second, among the host immune cells, we identified the CD68+ tumor-associated macrophages (TAMs) as the most common immune cell subset (14.5%, 154,899 cells). Three subsets of TAMs were identified: CD206+ M2-like (CD206+/CD163+/HLA-DR-/PDL1-), PDL1+ M2-like (PDL1+/CD11b+/CD206-/HLA-DR-), and HLA-DR+ M1-like (HLA-DR+/S100A4+/CD206-/PDL1-) (Fig. 1c-d). The expression of other macrophage markers aligned with this classification (Supp Fig 2c). Third, we defined three

subsets among the tumor-infiltrating CD8T cells (17,647 cells, 0.01%)- exhausted (PD1+/TIM3+/CD44-), effector (CD45RO+/CD44+/PD1-/TIM3-), or memory (CD45RO+/CD44-/PD1-) CD8T cells (Fig 1c-d). Thus, through CODEX analysis we classified discrete subsets of tumor cells, macrophages and CD8T cells (Fig 1d, Supp Table 2).

To validate our tumor and immune cell classification we used 3 approaches. First, we overlaid our unsupervised cell-calling on immunostained images and confirmed the accuracy of classification based on marker expression (Fig 1e). Second, we demonstrated a consistent proportion of immune and stromal cell types across various HCC clinical subgroups, indicating the reliability of the classification, with NASH-HCC notably displaying increased CD8T cell exhaustion as previously reported²⁵ (Supp Fig 3a-c). Third, we noted that the observed subset identification and proportion of macrophage and T-cell subsets are similar to prior reports²⁶⁻²⁸, However, we did note a higher proportion of neutrophils, possibly attributable to their underrepresentation in transcriptome-based deconvolution analyses^{29,30} (Supp Fig 4). Thus, our CODEX analysis provides an accurate and quantitative single-cell spatial profile of 20 major cell types in human HCC.

Residual human HCC has enrichment of Immunosuppressive cells

Next, we used the above single-cell phenotyping to identify differences in tumor and immune cell subsets that would distinguish primary and residual HCC. To study residual HCC, we identified patients with HCC who had undergone transarterial chemoembolization (mean of 2.42 cycles; SEM=1.32) and retained post-treatment viable HCC in the liver explant (n=55; 427,126 cells). For a comparative analysis with residual HCC, we included a control group of patients with treatment-naive primary HCC (n=53; 638,158 cells). The two groups were matched for key variables including age, sex, race, ethnicity, comorbidities, grade, microvascular invasion, AFP, BCLC stage and AJCC stage, but not matched for etiology and cirrhosis (Supp Table 3). We

could measure all 20 cell types in both residual and primary HCC. Thus, we could distinguish primary and residual HCC through their distinct distribution of cellular subtypes (Fig 2a-b).

We found higher infiltration of immunosuppressive tumor and immune cell subsets in residual HCC than in primary HCC. Specifically, PDL1+ macrophages ($p\text{Adj}=2.2\times 10^{-6}$), PDL1+ tumor cells ($p\text{Adj}=3.4\times 10^{-5}$), mast cells ($p\text{Adj}=3.1\times 10^{-4}$), exhausted CD8T cells ($p\text{Adj}=6.6\times 10^{-4}$) and NK cells ($p\text{Adj}=1.8\times 10^{-3}$) were more abundant in residual HCC (Fig 2c-e, Supp Fig 5a). Conversely, neutrophils ($p\text{Adj}=1.4\times 10^{-4}$) and fibroblasts ($p\text{Adj}=1.5\times 10^{-2}$) were relatively depleted in residual HCC compared to primary HCC (Fig 2c, Supp Fig 5b). Despite differences in the frequency of cirrhosis between primary and residual HCC, these observations remained consistent within the subgroup of HCCs arising in a cirrhotic background (Supp Fig 5c). Moreover, we show that M2-like macrophage enrichment was specific to the presence of therapy-resistant residual tumors post-TACE, rather than treatment effects, as evidenced by higher macrophage levels in TACE-refractory HCC³¹ compared to TACE-exposed peri-tumoral cirrhotic liver tissue (Supp Fig 6a-c) or sites of post-TACE complete response (Supp Fig 6d), with results being consistent across different TACE methods (Supp Fig 6e). Hence, residual HCC showed a more pro-tumor redistribution of specific cell types than primary HCC.

In addition to changes in cellular distribution, we observed four differences in cellular phenotype between residual and primary HCC. First, tumor cells in residual HCC showed a more stem-like ($\text{CD44}^{\text{high}}$, $\text{CK19}^{\text{high}}$) phenotype (Fig 2f). Second, the abundant PDL1+ macrophages within the residual HCC were more likely to be monocyte-derived ($\text{CD11b}^{\text{high}}$) and migratory ($\text{podoplanin}^{\text{high}}$) (Fig 2g). Third, the CD8T cells infiltrating residual HCCs were more exhausted, with higher PD1 and TIM3 expression (Fig 2h). Fourth, the NK cells present in residual HCCs were also dysfunctional, with higher levels of PD1 and TIM3 expression (Fig 2h). Thus, residual

HCC appears to be characterized by cancer stemness, enrichment of pro-tumor macrophages, and decreased immune surveillance associated with exhausted CD8T cells.

Spatial Interactions of Tumor and Immune Cells in Residual HCC Drive Immune evasion

We hypothesized that the differences observed between residual and tumor HCC in both the tumor and immune cellular subtypes may be related to direct interactions between tumor cells and host immune cells. To test this, we integrated single-cell phenotype data with spatial coordinates to analyze interactions between non-homotypic cells in direct contact with each other, that we defined as within a 25 μ m radius. Based on our results, we focused on examining interactions among tumor cells, macrophages, and CD8T cells.

We first compared the interactions of tumor cells in residual versus primary HCC (Fig 3a, Supp Fig 7a). The most significant change was seen in tumor cell interactions with PDL1+ macrophages (Fig 3b). In residual HCC, all four types of tumor cells we identified had more frequent direct interactions with PDL1+ macrophages compared to primary HCC (Fig 3b). This was true, whether tumors had high or low levels of PDL1+ macrophages (Supp Fig 7b). In contrast, tumor cells did not differentially interact with exhausted CD8T cells, despite the increased presence of the latter in residual HCC (Fig 3c). Among the interactions of tumor cells, those between EpCAM+ tumor cells and either M2-like PDL1+ or CD206+ macrophages were associated with poor recurrence-free survival in residual HCC (Fig 3d). We validated this finding in the TCGA cohort by showing that overexpression of genes representing the interaction between stem-like cancer cells (*EPCAM*, *KRT19*, *CD44*) and M2-like macrophages (*CD68*, *CD274*, *MRC1*, *CD163*) was indeed associated with a significantly poorer recurrence-free survival in HCC ($p=5.2\times 10^{-5}$) (Supp Fig 7c). Further, by employing 3D co-culture tumoroid *in vitro* experiments, we showed that co-culture of HCC cancer cells with M2-like polarized macrophages induced more cancer stemness than co-culture with M1-like macrophages (Supp

Fig 7d). Thus, in residual HCC, stem-like tumor cells appear to spatially interact with M2-like PDL1+ macrophages, and this interaction is associated with a worse clinical outcome.

Next, we focused on the interactions of macrophages (Supp Fig 7e). M2-like PDL1+ macrophages were found to more frequently directly interact with exhausted CD8T cells ($p=1.11\times10^{-3}$) (Fig 3e) but not effector ($p=0.17$) or memory CD8T cells ($p=0.38$) in residual HCC. These interactions of PDL1+ macrophages in residual HCC appeared to occur predominantly within fibrovascular bundles. PDL1+ macrophages interacted more frequently with both fibroblasts ($pAdj=2.99\times10^{-3}$), and endothelial cells ($p=7.7\times10^{-3}$) in residual HCC than primary HCC (Fig 3f). Similarly, we found that there was closer spatial proximity between PDL1+ macrophages and fibroblasts (44.99 vs. 179.75 μm ; $p = 0.027$) or endothelial cells (36.2 vs. 68.5 μm ; $p = 0.004$) in residual than primary HCC. This was not observed for the other two subsets of HLA-DR+ or CD206+ macrophages and fibroblasts (42.2 vs. 38.6 μm $p = 0.329$; 30.3 vs. 31.9, $p = 0.197$, respectively). Thus, in residual HCC, PDL1+ macrophages appear to directly interact with, and may result in the exhaustion of CD8T cells within fibrovascular bundles.

We next examined interactions that did not occur by direct contact but could still be mediated indirectly by intermediary cells. To first establish the range of indirect influence of a central cell, we developed a regression model (Supp Fig 8a). We found that the variance in a given central cell's expression of Ki67 and BCL2 could be explained by evaluating interaction radius ranging from 25 to 100 μm (Fig 3g, Supp Fig 8b). Based on this, we evaluated indirect interactions between non-homotypic cells lying between 25 μm and 100 μm of a given cell.

We found that in residual versus primary HCC, all four tumor cell subsets more frequently indirectly interacted with PDL1+ macrophages (Fig 3h, Supp Fig 8c-d). However, different from what we observed for direct interactions, we found that in residual HCC, the tumor cells did

indirectly interact more frequently with exhausted CD8T cells (Fig 3i). This raises the possibility that PDL1+ macrophages could serve as an intermediary facilitating indirect interactions between tumor cells and exhausted CD8T cells. Thus, residual HCC in contrast to primary HCC exhibits differences both in cellular composition, and in cellular direct and indirect interactions. This apparent remodeling of the cellular types and interactions in residual HCC amongst the stem-like tumor cells, PDL1+ macrophages, and exhausted CD8T cells could be responsible for changes in immune surveillance, as we explain more below.

Spatial Neighborhoods Reprogram Macrophages and CD8T Cells in Residual HCC

We wondered if the remodeling of cell-cell interactions in residual HCC had a higher-order spatial organization. To test this, we defined "cellular neighborhoods (CNs)" aiming to capture the intricate spatial arrangements within HCC as opposed to viewing them just as uniform sheets of cells. To determine these spatial CNs, we employed a previously reported approach that defined neighborhoods by clustering individual cells and their neighbors to identify broad patterns of spatial organization³² (Fig 4a). We identified nine distinct neighborhoods across all the HCC tissues (Fig 4b). Among these, four were tumor cell-dominant, four were immune cell-dominant, and one was of mixed cell population (termed "other", of unclear significance) (Fig 4b). Thus, through CN analysis, we delineated nine distinct neighborhoods of higher-order spatial organization within HCC.

To confirm we were identifying real spatial structures, we used three approaches. First, we overlaid the neighborhoods with H&E-stained sections and fluorescent images, confirming the accurate recapitulation of known spatial structures such as fibrovascular bundles and lymphoid infiltrates (Supp Fig 9a). Second, we observed the presence of these CNs in tumors across all stages, grades, and etiologies, suggesting their presence was a shared feature in the HCC microenvironment (Supp Fig 9b). Third, we confirmed that the canonical marker of the dominant

cell within each CN was indeed overexpressed in its respective CN (Supp Fig 9c). Thus, the microenvironment of HCC appears to be organized into spatial CNs.

We examined if the distribution of the identified spatial CNs was different between residual and primary HCCs (Fig 4c). Residual HCCs exhibited a higher prevalence of two neighborhoods, the M2-like macrophage immune CN ($p=4\times 10^{-5}$), and the vascular inflammatory tumor CN ($p=0.02$). In contrast, the CNs with abundant anti-tumor immune cells, the innate immune CN ($p=8.5\times 10^{-7}$), and T cell immune CN ($p=0.012$), were less frequent in residual HCC (Fig 4c). These findings show that in residual versus primary HCC there is a pro-tumor restructuring of the microenvironment.

We further examined the M2-like macrophage immune CN enriched in residual HCC. We hypothesized this CN may influence the cellular phenotype of tumor cells and T cells residing within it. The tumor cells residing in the M2-macrophage CN (17,046 cells, 7.4%) exhibited a more cancer stem-like ($CK19^{high}/EpCAM^{high}/CD44^{high}$), mesenchymal ($vimentin^{high}$), and pro-survival ($BCL2^{high}, Ki67^{high}$) phenotype than the tumor cells within another CN abundant in tumor cells but devoid of M2-like macrophages, the pauci-immune tumor CN (109,391 cells, 47.2%) (Fig 4d). Additionally, T cells within the M2-macrophage CN (4299 cells, 25.9%) exhibited a more exhausted phenotype ($PD1^{high}, TIM3^{high}, CD44^{low}, CD45RO^{low}$) than the T cells residing within another CN enriched in T-cells (8345 cells, 50.3%) (Fig 4d). The observations at the cellular level were also true at the tissue level. The residual HCC with higher M2-like macrophage CN had greater infiltration of EpCAM+ tumor cells and exhausted CD8T cells (Supp Fig 9d). Thus, M2-like macrophages appear to promote CD8T cell exhaustion within specific spatial CNs rather than across the entire tumor. This may facilitate immune evasion of stem-like tumor cells located within the M2-macrophage immune CN.

Next, we investigated the phenotype of macrophages and T cells residing within the two stem-like tumor cell CNs in residual HCC. Macrophages residing within the two stem-like tumor CNs were more likely to be M2-like ($CD206^{\text{high}}$, $CD163^{\text{high}}$), and CD8T cells more likely to be exhausted ($PD1^{\text{high}}$, $TIM3^{\text{high}}$), than in the other two non-stem-like tumor CNs (Fig 4d, Supp Fig 9e). Additionally, the abundance of EpCAM+-tumor CNs was associated with poor recurrence-free survival in residual HCC ($p=0.02$, HR 5.0) (Fig 4e). Taken together, these data indicate that the spatial organization into CNs is distinct in residual HCC than primary HCC. Specifically, the M2-macrophage CN and EpCAM+-tumor cell CN appear to promote spatially constrained CD8T cell exhaustion. This suggests that such spatial organization into M2-macrophage CN may serve as a mechanism by which residual tumor cells evade CD8T cell surveillance.

To experimentally test our observations from post-TACE residual human HCC, we conducted *in vitro* experiments to investigate how resistance to doxorubicin, the most commonly used chemotherapy agent in TACE, reprograms cancer cells and macrophages. Employing single-cell RNA sequencing, we analyzed 3D heterotypic tumoroids ($n=31,058$ cells) composed of either doxorubicin-resistant or control HCC cells (Fig 4f). In the doxorubicin resistant tumoroids, cancer cells demonstrated a stem-cell-like phenotype with higher expression of stemness, chemoresistance, and cytokines which can drive M2-like macrophage polarization (Supp Fig 10a-b). Further, doxorubicin resistant tumoroids were enriched in a specific macrophage cluster (C3) which showed a distinct M2-like phenotype, in contrast to the C4 cluster, which was depleted in doxorubicin resistant tumoroids ($CXCR4/LPLP^{\text{Hi}}$; $STAT1/ISG15^{\text{Lo}}$) (Fig 4g-h). Additionally, IF analysis confirmed that macrophages co-cultured with doxorubicin-resistant cancer cells exhibited PDL1 overexpression compared to those co-cultured with control cells ($p=1.6\times 10^{-6}$) (Fig 4i). In concordance, IF and flow cytometry analysis confirmed that monocyte-derived macrophages from patients with HCC treated with the conditioned media

from doxorubicin-resistant patient-derived tumoroids exhibited significantly higher PDL1 expression compared to those treated with conditioned media from control tumoroids ($p=1.6\times10^{-6}$) (Fig 4j, Supp Fig 10c) or with doxorubicin alone (Supp Fig 10d). Overall, our findings demonstrate that doxorubicin-resistant cancer cells not only adopt a more stem-cell-like phenotype but also significantly influence macrophage polarization towards an M2-like phenotype with elevated PDL1 expression.

TGF β pathway activation is a mechanism for persistence of residual tumor cells in HCC

To investigate the transcriptional changes within the tumor cell and macrophage neighborhoods identified by CODEX analysis, we used spatially resolved transcriptomics of residual HCC. We separately quantified the expression of 1812 tumor and immune-related genes within tumor-cell (pan CK+ve, CD45-/CD68-) and macrophage (pan CK-ve, CD45+/CD68+) areas of interest (AOIs) using Nanostring GeoMx DSP (Fig 5a-b). A total of 105 AOIs (tumor-cell ($n=53$) and macrophage ($n=52$) AOIs were included (patient details in Supp Table 4). The robustness of AOI classification was confirmed by canonical gene expression of each AOI (Fig 5c). We examined pathways activated within the AOIs of residual HCC compared to non-tumorous liver AOIs.

Residual HCC tumor-cell AOIs displayed upregulated immunosuppressive IL10 pathway ($p=4.7\times10^{-47}$) and PDL1 pathway ($p= 2.79\times10^{-37}$) (Supp Table 5)(Fig 5d). On the other hand, macrophage AOIs showed upregulated angiogenesis ($p= 3.75\times10^{-10}$) and invasiveness ($p= 8.33\times10^{-9}$) pathways (Supp Table 6) (Fig 5d). Thus, using spatial transcriptomics, we revealed distinct yet complementary pro-tumor pathway activation within the tumor-cell and macrophage AOIs of residual HCC.

To examine if transcriptional changes within tumor-cell or macrophage AOIs were prognostic, we established two gene signatures enriched in the respective AOIs of residual, but not primary HCC (Fig 5e). We applied the residual HCC tumor-cell and macrophage signatures to stratify

the independent cohort of human TCGA HCC (n=372). Enrichment of the macrophage signature was associated with poor overall- and recurrence-free survival on multivariable analysis of TCGA HCC, adjusting for age, sex, and tumor stage ($p=8.2\times 10^{-4}$, HR 1.9 [1.3-3.1]) (Fig 5f; Supp Fig 11a). In contrast, the tumor-cell signature did not show significant associations with overall or recurrence-free survival ($p=0.628$, HR 1.1 [0.8-1.6]) (Fig 5f; Supp Fig 11a). This suggests that macrophages, and not residual tumor cells alone, influence the trajectory of residual HCC towards recurrence and poor prognosis.

Next, we assessed upstream regulators of the molecular pathways activated within tumor-cell and macrophage AOIs. The receptor TGFBR1/2 kinase pathway was the top upstream regulator of the transcriptional changes in the tumor-cell AOIs ($p=3.1\times 10^{-44}$, z-score 2.5), while its corresponding ligand, *TGFB1* was the top upstream regulator of transcriptional changes in the macrophage AOIs of residual HCC ($p=2.7\times 10^{-9}$, z-score 1.2) (Fig 5g, Supp Fig 11b). Moreover, *TGFB1* was expressed at a higher level in the macrophage AOIs than tumor AOIs of residual HCC (Fig 5h). TGFB1 pathway effector gene *SMAD2* positively correlated with *CD274* (PDL1) within residual HCC, but not primary HCC (Fig 5i). Further, we used mRNA FISH to show that *TGFB1* mRNA expression was indeed higher in residual than primary HCC (Fig 5j). Additionally, multiplex FISH confirmed that the proportion of *TGFB1* expressing cells which were *CD68*⁺ macrophages was also higher in residual than primary HCC (Fig 5j). Collectively, our integration of CODEX and spatial transcriptomics analyses elucidates the central role of macrophage-mediated immunosuppressive pathways in residual tumor cell persistence. We propose that PDL1⁺ macrophages, identified to be enriched in residual HCC on CODEX analysis, may serve as a source for TGF β 1 pathway activation in residual tumor cells.

Transgenic mouse model of HCC demonstrates recurrence of HCC can arise from MRD

Our analysis of human residual HCC revealed a specific spatial organization of M2-like macrophages which potentially facilitates stem-like tumor cells to evade CD8T cell detection. We hypothesized this immune evasion is mediated by PDL1+ macrophages, which concurrently activate the TGF β 1 pathway in residual tumor cells, and also drive exhaustion of CD8T cells. We next sought to directly test this hypothesis using transgenic mouse models of HCC which retain residual dormant tumor cells after tumor regression.

To do this, we employed hepatocyte-specific transgenic mouse models of MYC-driven HCC, which express key HCC-specific genes and proteins, and show concordance with gene expression patterns in multiple human HCC datasets (Supp Fig 12). The non-metastatic MYC-HCC model has been previously reported to retain intrahepatic dormant residual tumor cells upon oncogene inactivation and tumor regression¹³. To more closely mimic human HCC and simulate disseminated residual tumors, we additionally employed the MYC/Twist1 model of metastatic HCC^{13,18} (MT-HCC). We now show that MT-HCC retains small clusters of hyperchromatic, non-proliferative (phospho histone3-ve), nonapoptotic (cleaved casp3-ve) viable residual tumor cells, both within the liver and at extrahepatic sites, upon oncogene inactivation (Fig 6a-b; Supp Fig 13a-b). Importantly, these areas of residual HCC are radiologically undetectable (Fig 6b), thus fulfilling criteria to be referred to as minimal residual disease (MRD)³³. Thus, our models effectively mimic the persistence of residual tumor cells post-tumor regression, as observed in post-TACE human residual HCC.

We evaluated if the MYC- and MT-HCC model are comparable to post-chemoembolization residual human HCC in four ways. First, we used time-series analysis to show that oncogene reactivation led to the recurrence of tumors from residual tumor cells within the regressed tumor

bed, recapitulating the clinical phenomenon of recurrence (Fig 6a-b). These recurrent tumors had shorter latency and poorer survival rates, pointing to their origin from MRD (Fig 6c). Second, we unambiguously traced the origin of recurrent tumors to MRD using a combination of subcutaneous transplantation studies and intravital microscopy to track live, residual RFP-labeled MT-HCC cells (Fig 6d). Third, we found the overexpression of a gene signature from mouse MRD was associated with poor overall- ($p=5.4\times 10^{-4}$, HR 1.8) and recurrence-free survival ($p=0.03$, HR 1.4) in the TCGA cohort of human HCC (Fig 6e). Fourth, we confirmed the translational relevance of our model to the context of chronic inflammation by demonstrating that tumor regression and MRD-driven recurrence also occur in the background of NASH induced by a high-fat diet. (Supp Fig 14). These results support the use of MYC- and MT-HCC mouse models for studying how MRD leads to recurrence in human HCC, and for evaluating therapies to prevent it.

Residual tumor cells in mouse MRD demonstrate cancer stemness

In our analysis of human HCC, we found that residual tumor cells exhibit cancer stem cell-like features. We characterized the *in vivo* residual tumor cells in our mouse models by performing scRNAseq of a microdissected tumor bed containing MRD ($n=15,300$ cells) (Fig 6f). A subset of cells ($n=355$, 0.02%) clustered with hepatocytes but differentially expressed several genes compared to the two main hepatocyte clusters (DEG 586 genes; 460 up, 126 down) (Fig 6f, Supp Table 7). Gene set enrichment analysis revealed these cells were transcriptionally analogous to embryonic stem cell lines (Fig 6g). Additionally, gene signatures associated with progenitor or cancer stem cells were enriched in the residual tumor cells (Fig 6g). Particularly, a gene signature representing liver cancer stem cell CK19+ tumors associated with human HCC recurrence³⁴ was strongly upregulated in this cluster ($p\text{Adj}=1.1 \times 10^{-11}$) (Fig 6g). Further, the residual tumor cells in the liver and metastatic sites expressed liver cancer stem cell markers

CD133 and CK19 (Supp Fig 15a-c). Thus, as seen in human post-chemoembolization residual tumor cells, the tumor cells in MRD in our mouse models exhibit cancer stemness.

Tgfβ pathway is activated in residual tumor cells in mouse models of MRD

Next, we found that the TGFβ pathway, identified as a key regulator of residual human HCC, was also activated in mouse MRD using three approaches. First, we show that the TGFβ pathway was the top activated upstream regulator of the transcriptional changes in MRD of both MYC- ($pAdj=1.8\times 10^{-50}$; enrichment score [ES] 6.6) and MT-HCC ($pAdj=7.9\times 10^{-49}$; ES 6.2) upon oncogene inactivation (Fig 6h). Second, we corroborated that the TGFβ pathway activation was specifically confined to a subset of stem-like tumor cells *in vitro* using scRNAseq (Supp Fig 16a-e). Third, we found that residual tumor cells *in vitro* have increased phosphorylation of Smad2/3 and reversible overexpression of the receptor *Tgfb1r1*, but did not express *Tgfb1* (Fig 6h-i). Thus, as we saw in the analysis of human post-TACE residual HCC, in our mouse model of MRD, the TGFβ pathway is activated in the residual tumor cells.

Mechanisms of Immune Evasion by Residual Tumor cells

We investigated if in our mouse models, as suggested by human residual HCC, macrophages within the MRD niche contribute to TGFβ activation in residual tumor cells (Fig 5g). Single-cell analysis of the *in vivo* mouse MRD demonstrated three distinct macrophage subsets (Fig 7a). Two macrophage subsets had a proinflammatory M1-like phenotype with higher expression of genes like *Il1r1*, *Cxcl1*, *Ido2*, and *Nlrp6* (Fig 7b). One of the macrophage clusters demonstrated an immunosuppressive phenotype ($n=1061$ cells) with overexpression *Cd274* (*Pdl1*) and enrichment of M2-like macrophage³⁵ and monocyte-derived macrophage gene signatures (DEG 979 genes; 669 up and 310 down) (Fig 7a-c, Supp Table 8). Moreover, this M2-like macrophage cluster expressed higher levels of *Tgfb1* ($pAdj=3.95\times 10^{-7}$). Thus, *Pdl1*^{high} macrophages appear to

be the source for the Tgf β pathway activation observed in residual tumor cells in our mouse models of MRD.

To see if these Pdl1^{high} macrophages spatially interact with residual tumor cells in mouse MRD, we used multiplex IF analysis. We confirmed that Pdl1^{high} macrophages were enriched in MRD and not in non-MRD bearing areas of the liver and also found that they closely interacted with stem-like residual tumor cells, both in the liver (Fig 7d) and the lungs (Supp Fig 17 a-b). Importantly, these Pdl1^{high} macrophages were confirmed to co-express Tgf β 1 (Fig 7e). To identify potential mechanisms of recruitment of these macrophages to MRD, we used a multiplex ELISA assay (Fig 7f) and phagocytosis assay (Fig 7g). We show that residual tumor cells, and not primary tumor cells, secrete four cytokines- Cxcl5, IL6, IL22 and IL18, which are known to promote M2-like macrophage polarization and increase PDL1 expression³⁶⁻³⁹ (Fig 7f). Also, macrophages exposed to media from residual tumor cells showed more impaired phagocytosis than those exposed to media from primary tumor cells (Fig 7g). Thus, residual tumor cells in our mouse models appear to use a cytokine-mediated mechanism to recruit Tgf β 1-secreting non-phagocytic Pdl1+ macrophages to MRD.

We examined T cell functionality within MRD using flow cytometry, given the established role of Pdl1+ macrophages in inducing T cell exhaustion^{40,41}. While infiltration of CD4T and CD8T cells, including naive, central memory, or effector phenotypes, were similar between MRD-bearing and control livers (Fig 7h, Supp Fig 18 a-b), we observed a significant enrichment of exhausted (Pd1+/Tim3+) CD8T cells in MRD-bearing liver (Fig 7h, Supp Fig 18 c-d). Thus, as we see in residual human HCC, in our mouse model of MRD we observed exhaustion of CD8T cells, suggesting this is a mechanism of impaired immune surveillance.

Combined blockade of Tgf β 1 and Pdl1 prevents HCC recurrence from MRD

Our analysis of human residual HCC and mouse MRD suggests that targeting the Tgf β 1 pathway and Pdl1^{High} macrophages could eliminate residual tumor cells and prevent tumor recurrence. To experimentally address this, we examined in our residual MYC-HCC or MT-HCC bearing transgenic mice, if a Tgfb1 inhibitor (Tgfb1l) or anti-Pdl1 antibody, either alone or in combination, prevented recurrence (Fig 8a). We confirmed the absence of macroscopic tumors by MRI imaging before randomizing transgenic mice with MRD to the 4 treatment groups (Fig 8a). Mice receiving combined anti Tgfb1l and Pdl1 therapy showed 8-fold reduction in recurrent tumor burden and a 5-fold reduction in recurrence rate, compared to control (both p<0.05, Fig 8b-c). These differences were also significant when compared with monotherapy with Tgfb1l or anti-Pdl1 (all p<0.05, Fig 8b-c). Combination anti Tgfb1l and Pdl1 therapy-treated livers demonstrated areas of higher CD4 and CD8T cell recruitment than either control or monotherapies (all p<0.05, Fig 8d). Moreover, CD4T and CD8T cells of mice treated with combination therapy were more activated (CD69+/CD44+) than the control group (Fig 8e). The combined inhibition of Tgfb1l and Pdl1 in a subcutaneous allograft model improved recurrence-free survival, confirming its effectiveness in preventing recurrence from MRD (Supp Fig 19a-d). Additionally, we found that combined inhibition of Tgfb1l and Pdl1 lacked efficacy in preventing the progression of primary MT-HCC, suggesting the mechanistic specificity to MRD (Supp Fig 19e-f). Thus, combined blockade of Tgf β 1 pathway and Pdl1 promoted recruitment and activation of T cell response and prevented tumor recurrence from MRD.

To determine if blocking Tgf β 1 and Pdl1 could eliminate MRD, we administered either control or Tgfb1l or anti-Pdl1 antibodies or their combination to mice bearing residual HCC and euthanized mice immediately after the completion of treatment, without reactivating the oncogenes (Fig 9a). Transgenic mice treated with the combination therapy exhibited increased recruitment of CD8T cells, and decreased Pdl1+ macrophages within MRD than treatment with control or the

respective monotherapies (Fig 9b-c). We also saw an increased number of apoptotic cells in MRD with combination therapy than control or monotherapies (Supp Fig 20a). Flow cytometry analysis confirmed that CD8T cells in mice treated with combination anti Tgfb1l/Pdl1 therapy were more activated (CD69+/CD44+) than with control (Supp Fig 20b). Hence, combined blockade of Tgf β and Pdl1 decreased immunosuppressive macrophage infiltration, elicited a robust CD8T cell response, eliminated MRD, and prevented HCC recurrence.

We note that our transgenic mouse models of MRD recapitulate the natural history of oncogene-deprived residual tumor cell persistence and HCC recurrence, but they do not involve persistence of residual tumors after exposure to therapeutic agents like doxorubicin, as is used in TACE for human HCC⁴². Hence, we complemented our MRD mouse model by developing a immunocompetent mouse model of syngeneic orthotopic allografts in wild-type C57/BL6 mice with Hep53.4 HCC cells that underwent *in vitro* selection to be either doxorubicin-resistant or control (Fig 9d Supp Fig 21a). Treatment with either control or combined Tgfb1l and anti-Pdl1 antibodies in the doxorubicin-resistant orthotopic allografts resulted in a significant reduction in liver tumor burden ($p=0.01$) (Fig 9e-f). Immune analysis revealed increased CD8T cell infiltration, elimination of PDL1+/CD206+ M2-like macrophages and increased infiltration of CD86+/MHCII+ M1-like macrophages (Fig 9e-h). In contrast, control allografts showed no significant response to this treatment (Fig 9e-f, Supp Fig 21b-d). These observations confirm findings from our transgenic MRD model, highlighting the complementary nature of both models and underscoring the therapeutic potential of dual Tgf β 1 and Pdl1 blockade in eliminating both oncogene-deprived stem-like MRD and doxorubicin-resistant murine HCC.

DISCUSSION

We combined spatial analysis of both human clinical samples and transgenic mouse models of HCC to determine the mechanism of persistence of residual disease in HCC, and suggest a possible therapeutic approach to improve clinical outcome. We identified that interactions between stem-like tumor cells and immunosuppressive PDL1+ macrophages within spatially constrained neighborhoods, in both human and mouse residual HCC, were linked to CD8T cell exhaustion and immune evasion. Further, macrophage-mediated TGF β pathway activation within residual tumor cells was found to enable persistence of both human and mouse MRD. Finally, we provide preclinical evidence that combined inhibition of PDL1+ macrophage-mediated TGF β activation eliminates MRD in mouse HCC and prevents recurrence. Our results provide mechanistic insight that suggests a therapeutic strategy for eliminating residual disease to prevent cancer recurrence.

We harness the power of multiple complementary spatial biology technologies to create a high-resolution spatial map of residual human HCC. Notably, residual disease that persists after therapy is a poorly characterized entity, especially in human solid tumors, due to challenges in detecting these areas. A few recent studies have employed single-cell RNA sequencing of primary HCC^{43–45} or CODEX of treatment-naive HCC^{46,47}, however, the spatial organization of post-TACE residual HCC is not known. Our spatial mapping provides three key insights. First, spatial interactions of cancer stem cells and pro-tumor M2-like macrophages are critical drivers of recurrence in residual HCC, rather than just the abundance of these cells, as previously suggested^{48–50}. Second, monocyte-derived PDL1+ macrophages are recruited to residual HCC and are associated with exhaustion of CD8T cells^{40,51,52}, a finding that adds a new dimension to their known role in cancer progression^{53–55}. Third, the spatial organization of residual HCC into M2-like macrophage enriched neighborhoods, where CD8T cells are rendered exhausted, allows stem-like tumor cells within these constrained areas to evade immune detection. Thus,

our spatial analysis identified tumor cell and host immune cell interactions that could enable evasion of immune surveillance and eventual tumor recurrence of HCC.

We experimentally examined the mechanisms of MRD in HCC using transgenic mouse models^{13,18}. Previous studies have analyzed MRD in HCC using xenografts in immunocompromised hosts^{56–58}. In contrast, our transgenic mouse models enable *in situ* study of naturally arising tumors in hosts with an intact immune system. A MRD-HCC signature derived from the transgenic models was indicative of shorter recurrence-free survival, affirming their relevance to human HCC. In these models, we identify that stem-like tumor cells reversibly overexpress Tgfb1, and spatially interact with the Tgfβ1-secreting Pdl1+ macrophages abundant in MRD. Further, blocking the Tgfβ pathway alone was not effective in preventing HCC recurrence. Rather, the concordant elimination of macrophages, which are a source of Tgfb1, with Pdl1 blockade, was required to induce a robust T cell response, eliminate residual tumor cells, and prevent recurrence. Additionally, we validated the therapeutic efficacy of this combination in an immunocompetent mouse model of doxorubicin-resistant HCC. Combined blockade of TGFβ1 and PDL1 has been trialed in primary cancers^{59–61}, yielding inconsistent results⁶² and exhibiting toxicity with extended use. Our study suggests that targeting MRD through brief adjuvant therapy can mitigate limitations seen in prior trials and potentially prevent HCC recurrence.

Our study creates a unique comprehensive single-cell spatial map of post-chemoembolization residual human HCC, revealing critical interactions among stem-like tumor cells, M2-like macrophages, and exhausted CD8T cells, insights gained only by preserving spatial context. Moreover, using a transgenic mouse model for disseminated MRD we demonstrate that the insights gained from spatial analysis can indeed be actionable, thus guiding us to target Tgfβ and Pdl1 to eliminate MRD in HCC. Thus, our results suggest a new adjuvant therapeutic strategy for reducing recurrence in HCC and improving patient outcomes.

METHODS

Patient Cohort Selection

In this study, we identified two cohorts of patients diagnosed with HCC who met the following inclusion criteria. For cohort 1 (residual HCC)- patients with a histologically confirmed diagnosis of HCC, underwent liver transplantation, received bridging therapy with transarterial chemoembolization (TACE), and had viable residual HCC in the explanted liver tissue. Additional criteria included availability of sufficient tissue in formalin-fixed paraffin-embedded (FFPE) blocks, we carefully selected those nodules which had been targeted for TACE and ensured adequate samples for our downstream analysis. Exclusion criteria included a history of other malignancies, receipt of resection prior to liver transplantation, receipt of Y90 or radiation therapy prior to transplant or evidence of metastatic cancer. All patients in this cohort had received doxorubicin-based TACE- a majority of which was DEB-TACE with doxorubicin eluting beads (n=102, 89%) and a smaller proportion received conventional TACE (n=14, 11%), none had received bland TACE. A consistent team of experienced interventional radiologists at a single institution performed all TACE procedures. Patients undergoing TACE underwent follow-up CT or MRI scans 8-12 weeks post-procedure to assess therapeutic response, which was evaluated using the modified Response Evaluation Criteria in Solid Tumors (mRECIST) system⁶³. Decisions regarding additional TACE treatments were made during multidisciplinary tumor board meetings. For the control group (primary HCC), we selected patients who underwent surgical resection for HCC and had not received any locoregional therapy or systemic therapy prior to HCC. Additionally, similar to cohort 1, these patients did not have any other form of cancer or metastatic tumors. In both groups, we collected comprehensive clinical and pathological data, including patient demographics, tumor characteristics, details of the treatments received, and outcomes following the treatment.

CODEX multiplex staining and analysis- A 41-plex custom CODEX antibody panel was developed and validated (Enable Medicine, Menlo Park, CA, USA) for ultra-highplex imaging utilizing purified, carrier-free antibodies conjugated to unique DNA oligonucleotide barcodes (Akoya Biosciences, Menlo Park, CA, USA) (Supp table 1). Image processing and analysis were performed as described before³². Further details are provided in the supplementary methods.

Nanostring Digital Spatial Profiling- We used the published experimental methods for the Nanostring GeoMx analysis¹⁹. The GeoMx Digital Spatial Profiling instrument from NanoString Technologies, Inc. (Seattle, WA) was used for immunofluorescence imaging. Details regarding the procedure are provided in the supplementary methods. Differential gene expression and gene set enrichment analysis were performed in the Omics Explorer software from QluCore (Lund, Sweden). The Benjamini-Hochberg correction was used to decrease the false discovery rate. Principal component analysis was conducted. Upstream regulators of transcription were discovered using the Ingenuity Pathway Analysis software (Aarhus, Denmark).

Transgenic Mice and In vivo Treatment- Animals were housed in a pathogen-free environment at Stanford University and all procedures were performed in accordance with Stanford's Administrative Panel on Laboratory Animal Care (APLAC) protocols. LAP-tTA/tet-O-MYC and LAP-tTA/TRE-*Twist1*/Luc transgenic lines were used, as previously described¹³. Littermate controls were used for all experiments. Mice were administered weekly doses of 0.1 mg/mL doxycycline (Sigma) in drinking water during mating and until four weeks of age. At 4 weeks, mice were taken off doxycycline. Mice were screened for tumors via MRI at approximately 2-3 months of age, at which time they developed tumors between 50-150 mm³. Once liver tumors and/or lung metastases were confirmed, mice were placed on doxycycline to induce tumor regression. MRI was used to confirm complete tumor regression. To induce tumor recurrence, mice were taken off doxycycline and monitored closely. MRI was used to confirm

complete tumor regression. Two weeks following complete radiologic tumor resolution, mice were enrolled into one of four treatment groups and treated for two weeks (Fig 8a). Control Rat IgG (BioXCell) and αPDL1 (clone 10 F.9G2, BioXCell) antibodies were given I.P. (100 µg/mouse) every other day. The TGFBR1 inhibitor SB431542 was dosed 10 mg/kg (dissolved in DMSO) daily intraperitoneally as previously described⁶⁴. At the end of treatment, mice were taken off doxycycline and monitored for tumor recurrence with MRI.

Establishment and Treatment of immunocompetent syngeneic allograft models of HCC

The murine HCC cell line Hep 53.4⁶⁵ derived from HCC arising in the C57/BL6 background was used to establish orthotopic syngeneic allografts. The cells were cultured in DMEM, 10% v/v serum, 2 mM L-glutamine and antibiotics in a humidified atmosphere of 5% CO₂ at 37°C. Cells were tested negative for mycoplasma contamination. Cells were cultured in the presence of increasing concentrations of doxorubicin for 96 hrs to determine an IC50 of 1µM. Clones of cells that remained viable after doxorubicin treatment or cells exposed to control treatment for 96 hours were used to create orthotopic allografts. C57Bl/6J mice at 6–8 weeks old were purchased from Jackson Laboratories and maintained in accordance with the APLAC protocol. A total of 3×10^6 cells in 40 µl of a Matrigel (Corning) and phosphate-buffered saline (PBS) mixture per mouse were injected orthotopically into the left lobe of the livers of mice as previously described^{66,67}. Two weeks after engraftment, mice were enrolled into two treatment groups and treated for two weeks (Fig 9d). Control Rat IgG (BioXCell) and αPDL1 (clone 10 F.9G2, BioXCell) antibodies were given I.P. (100 µg/mouse) every other day. The Tgfbr1 inhibitor SB431542 was dosed 10 mg/kg (dissolved in DMSO) daily intraperitoneally as previously described⁶⁴. At the end of treatment, mice were euthanized and evaluated for treatment response.

Statistical analysis- Differences between groups were analyzed using Student's t-test or one-way analysis of variance (ANOVA). The Benjamini-Hochberg method was used for adjusting p values. Chi-square test was used to compare categorical variables. Kaplan Meier analysis with the Log Rank test was performed for survival analysis. All graphs are presented as the mean +/- SEM. An adjusted P value of less than 0.05 was considered to be significant.

More detailed methods are presented in the Supplementary Methods section.

ACKNOWLEDGEMENTS

RD- National Institutes of Health (NIH) grant CA222676 from the National Cancer Institute (NCI), American College of Gastroenterology Junior Faculty Career Development Grant, Cancer League Award.

DF- National Institutes of Health (NIH) grant CA208735 and CA253180 from the National Cancer Institute (NCI).

Pauline Chu- Helped with mouse histology services.

DATA AVAILABILITY STATEMENT

All CODEX images will be made available at <https://app.enablemedicine.com/portal/visualizer>.

The link comes with an easy-to-use interface that allows for easy examination of the data upon registration.

The mouse single cell and whole transcriptome sequencing data generated in this study will be publicly available in the NCBI GEO database <https://www.ncbi.nlm.nih.gov/geo/> accession GSE243176 and GSE242746.

Publicly available TCGA liver cancer data was used for analysis from https://www.cbiportal.org/study/summary?id=lihc_tcga_pan_can_atlas_2018.

Here are the tokens for the sequencing data submitted to GEO-

GSE243176: izyzoegcxrorhoj

GSE242745: itkbwecgllihvgz

GSE242743: opqhmssiphqbhol

CODE AVAILABILITY STATEMENT

No custom code or algorithm used.

REFERENCES

1. Lee, Y.-T. *et al.* The Mortality and Overall Survival Trends of Primary Liver Cancer in the United States. *J. Natl. Cancer Inst.* **113**, 1531–1541 (2021).
2. Lei, J. *et al.* Response to transarterial chemoembolization may serve as selection criteria for hepatocellular carcinoma liver transplantation. *Oncotarget* **8**, 91328–91342 (2017).
3. Kim, D. J. *et al.* Recurrence of hepatocellular carcinoma: importance of mRECIST response to chemoembolization and tumor size. *Am. J. Transplant* **14**, 1383–1390 (2014).
4. Agopian, V. G. *et al.* Impact of Pretransplant Bridging Locoregional Therapy for Patients With Hepatocellular Carcinoma Within Milan Criteria Undergoing Liver Transplantation: Analysis of 3601 Patients From the US Multicenter HCC Transplant Consortium. *Ann. Surg.* **266**, 525–535 (2017).
5. Adeniji, N. *et al.* Impact of Bridging Locoregional Therapies for Hepatocellular Carcinoma on Post-transplant Clinical Outcome. *Clin. Transplant.* **34**, e14128 (2020).
6. Ghajar, C. M. Metastasis prevention by targeting the dormant niche. *Nat. Rev. Cancer* **15**, 238–247 (2015).
7. Cable, J. *et al.* Cancer stem cells: advances in biology and clinical translation-a Keystone Symposia report. *Ann. N. Y. Acad. Sci.* **1506**, 142–163 (2021).
8. Cole, A. J., Fayomi, A. P., Anyaeche, V. I., Bai, S. & Buckanovich, R. J. An evolving paradigm of cancer stem cell hierarchies: therapeutic implications. *Theranostics* **10**, 3083–3098 (2020).
9. Lee, T. K.-W., Guan, X.-Y. & Ma, S. Cancer stem cells in hepatocellular carcinoma - from origin to clinical implications. *Nat. Rev. Gastroenterol. Hepatol.* **19**, 26–44 (2022).
10. Price, T. T. *et al.* Dormant breast cancer micrometastases reside in specific bone marrow niches that regulate their transit to and from bone. *Sci. Transl. Med.* **8**, 340ra73 (2016).
11. Gilbertson, R. J. & Graham, T. A. Cancer: Resolving the stem-cell debate. *Nature* vol. 488

- 462–463 (2012).
12. Lan, L. & Behrens, A. Are There Specific Cancer Stem Cell Markers? *Cancer Res.* **83**, 170–172 (2023).
 13. Shachaf, C. M. *et al.* MYC inactivation uncovers pluripotent differentiation and tumour dormancy in hepatocellular cancer. *Nature* **431**, 1112–1117 (2004).
 14. Ding, W. *et al.* Clinicopathologic and prognostic significance of tumor-associated macrophages in patients with hepatocellular carcinoma: A meta-analysis. *PLoS One* **14**, e0223971 (2019).
 15. Zhu, X.-D. *et al.* High expression of macrophage colony-stimulating factor in peritumoral liver tissue is associated with poor survival after curative resection of hepatocellular carcinoma. *J. Clin. Oncol.* **26**, 2707–2716 (2008).
 16. Borriello, L. *et al.* Primary tumor associated macrophages activate programs of invasion and dormancy in disseminating tumor cells. *Nat. Commun.* **13**, 626 (2022).
 17. Dhanasekaran, R. *et al.* MYC Overexpression Drives Immune Evasion in Hepatocellular Carcinoma That Is Reversible through Restoration of Proinflammatory Macrophages. *Cancer Res.* **83**, 626–640 (2023).
 18. Dhanasekaran, R. *et al.* and cooperate to drive metastasis by eliciting crosstalk between cancer and innate immunity. *Elife* **9**, (2020).
 19. Merritt, C. R. *et al.* Multiplex digital spatial profiling of proteins and RNA in fixed tissue. *Nat. Biotechnol.* **38**, 586–599 (2020).
 20. Zollinger, D. R., Lingle, S. E., Sorg, K., Beechem, J. M. & Merritt, C. R. GeoMxTM RNA Assay: High Multiplex, Digital, Spatial Analysis of RNA in FFPE Tissue. *Methods Mol. Biol.* **2148**, 331–345 (2020).
 21. Black, S. *et al.* CODEX multiplexed tissue imaging with DNA-conjugated antibodies. *Nat. Protoc.* **16**, 3802–3835 (2021).
 22. Uenishi, T. *et al.* Cytokeratin 19 expression in hepatocellular carcinoma predicts early

- postoperative recurrence. *Cancer Sci.* **94**, 851–857 (2003).
23. Khosla, R. *et al.* EpCAM+ Liver Cancer Stem-Like Cells Exhibiting Autocrine Wnt Signaling Potentially Originate in Cirrhotic Patients. *Stem Cells Transl. Med.* **6**, 807–818 (2017).
24. Liu, C.-Q. *et al.* Expression patterns of programmed death ligand 1 correlate with different microenvironments and patient prognosis in hepatocellular carcinoma. *Br. J. Cancer* **119**, 80–88 (2018).
25. Pfister, D. *et al.* NASH limits anti-tumour surveillance in immunotherapy-treated HCC. *Nature* **592**, 450–456 (2021).
26. Comprehensive and Integrative Genomic Characterization of Hepatocellular Carcinoma. *Cell* **169**, 1327–1341.e23 (2017).
27. Guo, Y. *et al.* The Heterogeneity of Immune Cell Infiltration Landscape and Its Immunotherapeutic Implications in Hepatocellular Carcinoma. *Front. Immunol.* **13**, 861525 (2022).
28. Yu, S. *et al.* Tumor-infiltrating immune cells in hepatocellular carcinoma: Tregs is correlated with poor overall survival. *PLoS One* **15**, e0231003 (2020).
29. Veglia, F. *et al.* Analysis of classical neutrophils and polymorphonuclear myeloid-derived suppressor cells in cancer patients and tumor-bearing mice. *J. Exp. Med.* **218**, (2021).
30. Salcher, S. *et al.* High-resolution single-cell atlas reveals diversity and plasticity of tissue-resident neutrophils in non-small cell lung cancer. *Cancer Cell* **40**, 1503–1520.e8 (2022).
31. Singal, A. G. *et al.* AASLD Practice Guidance on prevention, diagnosis, and treatment of hepatocellular carcinoma. *Hepatology* **78**, 1922–1965 (2023).
32. Schürch, C. M. *et al.* Coordinated Cellular Neighborhoods Orchestrate Antitumoral Immunity at the Colorectal Cancer Invasive Front. *Cell* **183**, 838 (2020).
33. Dasari, A., Grothey, A. & Kopetz, S. Circulating Tumor DNA-Defined Minimal Residual Disease in Solid Tumors: Opportunities to Accelerate the Development of Adjuvant

- Therapies. *J. Clin. Oncol.* **36**, JCO2018789032 (2018).
34. Villanueva, A. *et al.* Combining clinical, pathology, and gene expression data to predict recurrence of hepatocellular carcinoma. *Gastroenterology* **140**, 1501–12.e2 (2011).
 35. Pello, O. M. *et al.* Role of c-MYC in alternative activation of human macrophages and tumor-associated macrophage biology. *Blood* **119**, 411–421 (2012).
 36. Li, Z. *et al.* Cancer-associated fibroblasts promote PD-L1 expression in mice cancer cells via secreting CXCL5. *Int. J. Cancer* **145**, 1946–1957 (2019).
 37. Zhang, W. *et al.* IL-6 promotes PD-L1 expression in monocytes and macrophages by decreasing protein tyrosine phosphatase receptor type O expression in human hepatocellular carcinoma. *J Immunother Cancer* **8**, (2020).
 38. Xi, X. *et al.* Interleukin-22 promotes PD-L1 expression via STAT3 in colon cancer cells. *Oncol. Lett.* **22**, 716 (2021).
 39. Kobori, T. *et al.* Interleukin-18 Amplifies Macrophage Polarization and Morphological Alteration, Leading to Excessive Angiogenesis. *Front. Immunol.* **9**, 334 (2018).
 40. Petty, A. J. *et al.* Hedgehog-induced PD-L1 on tumor-associated macrophages is critical for suppression of tumor-infiltrating CD8+ T cell function. *JCI Insight* **6**, (2021).
 41. Peranzoni, E. *et al.* Macrophages impede CD8 T cells from reaching tumor cells and limit the efficacy of anti-PD-1 treatment. *Proc. Natl. Acad. Sci. U. S. A.* **115**, E4041–E4050 (2018).
 42. Patel, M. & Pillai, A. Management of Intermediate-Stage Hepatocellular Carcinoma: Systemic Versus Locoregional Therapy. *Surg. Oncol. Clin. N. Am.* **33**, 159–172 (2024).
 43. Lu, Y. *et al.* A single-cell atlas of the multicellular ecosystem of primary and metastatic hepatocellular carcinoma. *Nat. Commun.* **13**, 4594 (2022).
 44. Ma, L. *et al.* Single-cell atlas of tumor cell evolution in response to therapy in hepatocellular carcinoma and intrahepatic cholangiocarcinoma. *J. Hepatol.* **75**, 1397–1408 (2021).
 45. Ma, L. *et al.* Tumor Cell Biodiversity Drives Microenvironmental Reprogramming in Liver

- Cancer. *Cancer Cell* **36**, 418–430.e6 (2019).
46. Ruf, B. *et al.* Tumor-associated macrophages trigger MAIT cell dysfunction at the HCC invasive margin. *Cell* **186**, 3686–3705.e32 (2023).
 47. Maestri, E. *et al.* Spatial proximity of Tumor-Immune interactions predicts patient outcome in hepatocellular carcinoma. *Hepatology* (2023) doi:10.1097/HEP.0000000000000600.
 48. Govaere, O. *et al.* Keratin 19: a key role player in the invasion of human hepatocellular carcinomas. *Gut* **63**, 674–685 (2014).
 49. Zhang, J. *et al.* Overexpression of Epcam and CD133 Correlates with Poor Prognosis in Dual-phenotype Hepatocellular Carcinoma. *J. Cancer* **11**, 3400–3406 (2020).
 50. Noh, C.-K. *et al.* EpCAM as a Predictive Marker of Tumor Recurrence and Survival in Patients Who Underwent Surgical Resection for Hepatocellular Carcinoma. *Anticancer Res.* **38**, 4101–4109 (2018).
 51. Huang, Y.-K. *et al.* Macrophage spatial heterogeneity in gastric cancer defined by multiplex immunohistochemistry. *Nat. Commun.* **10**, 3928 (2019).
 52. Liu, Y. *et al.* Immune Cell PD-L1 Colocalizes with Macrophages and Is Associated with Outcome in PD-1 Pathway Blockade Therapy. *Clin. Cancer Res.* **26**, 970–977 (2020).
 53. Zhou, C. *et al.* Disruption of SLFN11 Deficiency-Induced CCL2 Signaling and Macrophage M2 Polarization Potentiates Anti-PD-1 Therapy Efficacy in Hepatocellular Carcinoma. *Gastroenterology* **164**, 1261–1278 (2023).
 54. Murai, H. *et al.* Multiomics identifies the link between intratumor steatosis and the exhausted tumor immune microenvironment in hepatocellular carcinoma. *Hepatology* **77**, 77–91 (2023).
 55. Li, X. *et al.* Targeting of tumour-infiltrating macrophages via CCL2/CCR2 signalling as a therapeutic strategy against hepatocellular carcinoma. *Gut* **66**, 157–167 (2017).
 56. Martin-Padura, I. *et al.* Residual dormant cancer stem-cell foci are responsible for tumor relapse after antiangiogenic metronomic therapy in hepatocellular carcinoma xenografts.

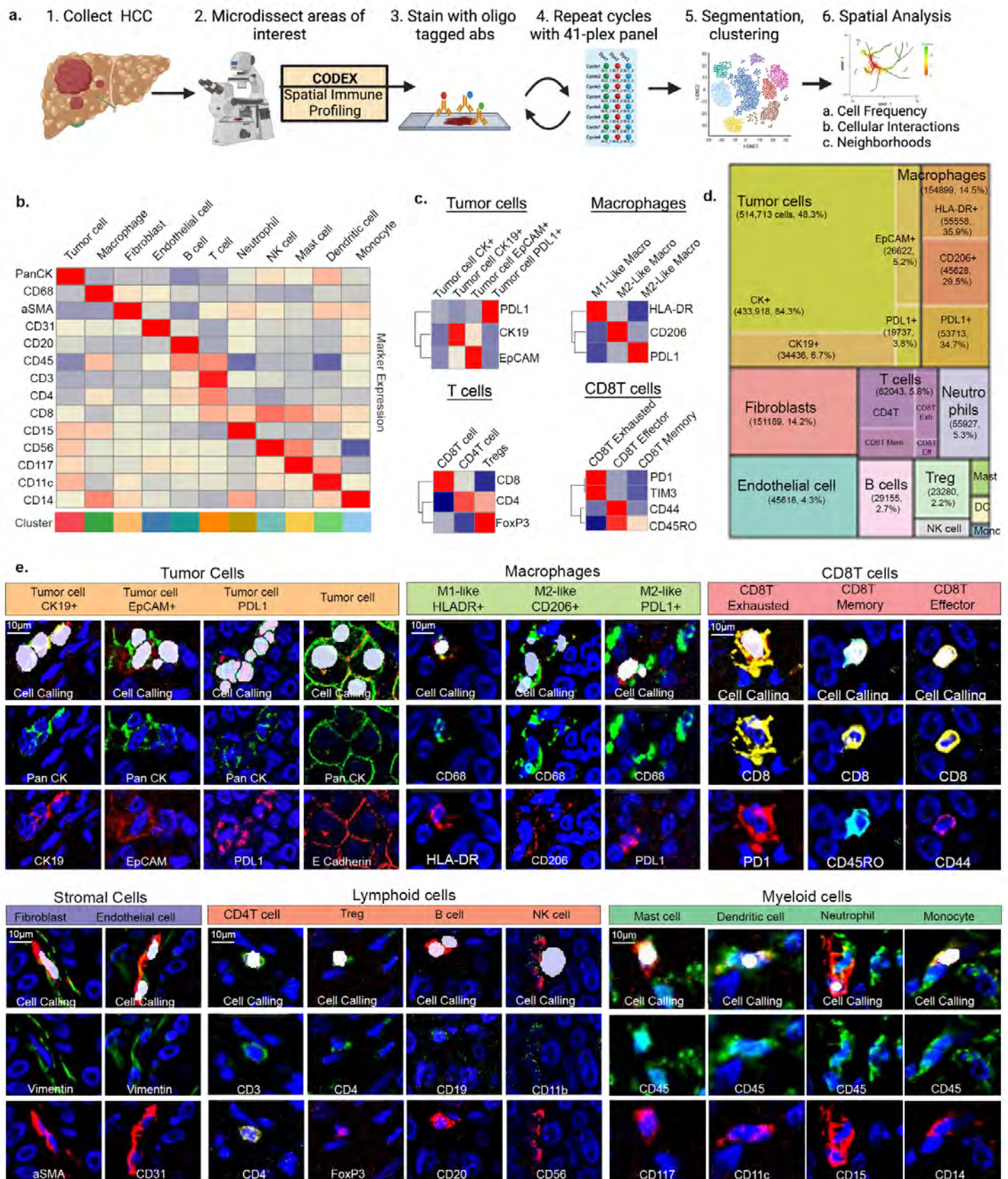
- Lab. Invest.* **92**, 952–966 (2012).
57. Haraguchi, N. *et al.* CD13 is a therapeutic target in human liver cancer stem cells. *J. Clin. Invest.* **120**, 3326–3339 (2010).
 58. Schrader, J. *et al.* Matrix stiffness modulates proliferation, chemotherapeutic response, and dormancy in hepatocellular carcinoma cells. *Hepatology* **53**, 1192–1205 (2011).
 59. Ravi, R. *et al.* Bifunctional immune checkpoint-targeted antibody-ligand traps that simultaneously disable TGF β enhance the efficacy of cancer immunotherapy. *Nat. Commun.* **9**, 741 (2018).
 60. Mariathasan, S. *et al.* TGF β attenuates tumour response to PD-L1 blockade by contributing to exclusion of T cells. *Nature* **554**, 544–548 (2018).
 61. Lan, Y. *et al.* Enhanced preclinical antitumor activity of M7824, a bifunctional fusion protein simultaneously targeting PD-L1 and TGF- β . *Sci. Transl. Med.* **10**, (2018).
 62. Metropulos, A. E., Munshi, H. G. & Principe, D. R. The difficulty in translating the preclinical success of combined TGF β and immune checkpoint inhibition to clinical trial. *EBioMedicine* **86**, 104380 (2022).
 63. Lencioni, R. & Llovet, J. M. Modified RECIST (mRECIST) assessment for hepatocellular carcinoma. *Semin. Liver Dis.* **30**, 52–60 (2010).
 64. Wang, S. K., Xue, Y. & Cepko, C. L. Microglia modulation by TGF- β 1 protects cones in mouse models of retinal degeneration. *J. Clin. Invest.* **130**, 4360–4369 (2020).
 65. Kress, S. *et al.* p53 mutations are absent from carcinogen-induced mouse liver tumors but occur in cell lines established from these tumors. *Mol. Carcinog.* **6**, 148–158 (1992).
 66. Brown, Z. J., Heinrich, B. & Greten, T. F. Establishment of Orthotopic Liver Tumors by Surgical Intrahepatic Tumor Injection in Mice with Underlying Non-Alcoholic Fatty Liver Disease. *Methods Protoc* **1**, (2018).
 67. Zabransky, D. J. *et al.* Profiling of syngeneic mouse HCC tumor models as a framework to understand anti-PD-1 sensitive tumor microenvironments. *Hepatology* **77**, 1566–1579

(2023).

Main Figures

*Multi-omic Spatial Analysis Reveals Targetable Macrophage-Mediated Mechanisms of Immune Evasion in
Hepatocellular Carcinoma Minimal Residual Disease*

FIGURE 1 High dimensional single-cell spatial atlas of the tumor immune microenvironment in HCC

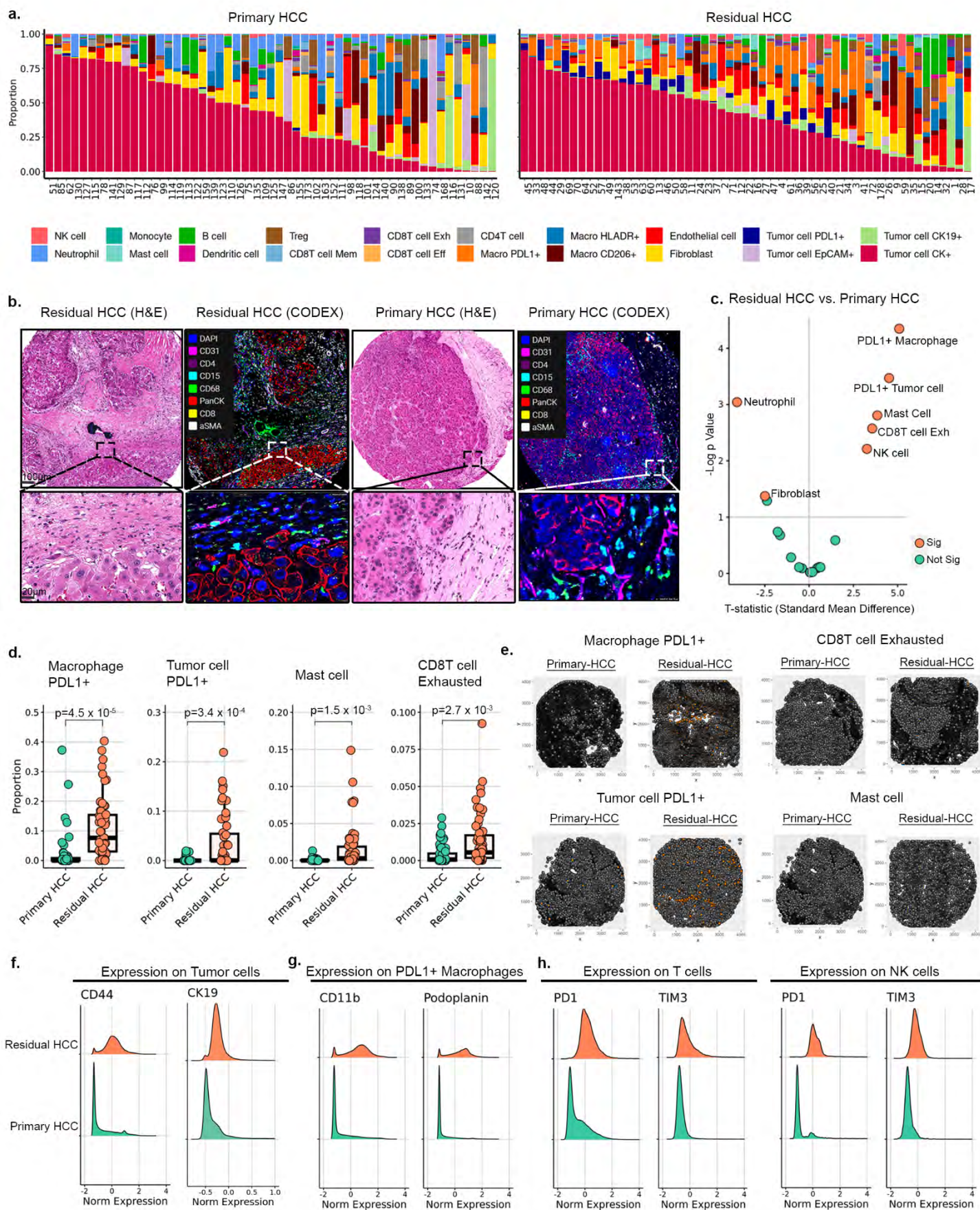


- Single-cell spatial analysis workflow of human HCC tumor cores using CODEX to determine cell frequency, cell-cell interactions, and cellular neighborhoods
- Heat map dendrogram of unsupervised clustering using canonical marker expression to define major tumor and immune cell subsets. Heatmap scaled by column.

- c. Sub-classification of tumor cells, macrophages and T cells using cell-specific canonical markers. Heatmap is scaled by row.
- d. Graphical representation of the 20 cell types and subtypes with their absolute cell counts and proportions in the CODEX dataset.
- e. CODEX imaging representations of the canonical markers used to verify the validity of the unsupervised clustering for each cell type. The cell-type (white filling) is overlaid on the immunostained images.

Abbreviations: abs- antibodies, CODEX-co-detection by indexing, HCC- hepatocellular carcinoma, PanCK-pan-cytokeratin, CK19- cytokeratin 19, EPCAM- epithelial cellular adhesion molecule, PDL1- programmed death ligand 1, PD1- programmed cell death protein 1, CD- cluster of differentiation, HLA-DR-human leukocyte antigen, DR isotype, TIM3- T cell immunoglobulin and mucin domain-containing protein 3, DC-dendritic cell, NK-natural killer, Treg- regulatory T cell, Exh- Exhausted, Eff- Effector.

FIGURE 2 Immunosuppressive Cell Enrichment and Tissue Remodeling in Residual HCC

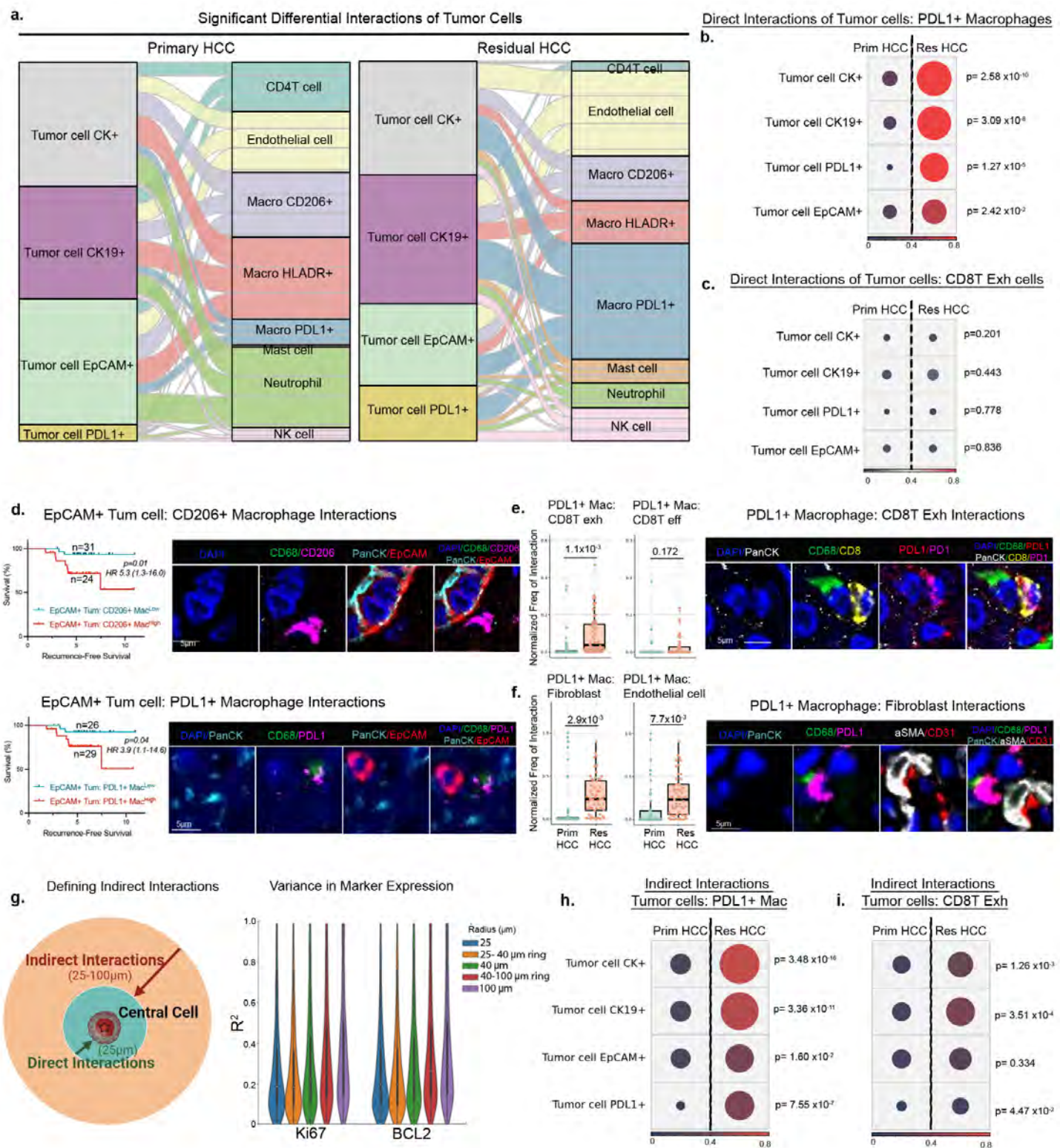


- a. Immune and tumor cell proportions in residual HCCs from chemotherapy-treated liver explants (residual HCC, n=55) compared to primary resected primary HCC (n = 53).
- b. H&E and CODEX imaging representations of a residual and primary HCC tumor core. In each CODEX image, eight canonical markers (DAPI, CD31, CD4, CD15, CD68, PanCK, CD8, and aSMA) are overlaid onto the image in different colors.
- c. Volcano plot showing the differential enrichment of tumor and immune cell populations (with statistical significance; shown with Bonferroni correction for multiple comparisons) in residual (n=55) vs primary HCCs (n=53).
- d. Proportion of PDL1+ macrophages, PDL1+ tumor cells, mast cells, and exhausted T cells in residual (n=55) vs primary HCCs (n=53).
- e. Representative Voronoi plot of cores showing PDL1+ macrophage, PDL1+ tumor cells, mast cells, and exhausted T cells density in residual (n=55) vs primary HCCs (n=53).
- f. Comparison of normalized expression of stemness marker CD44 and CK19 marker in tumor cells from residual (n=217,105) and primary HCC (n=297,608) (both pAdj value <3.0x10⁻³⁰⁰).
- g. Comparison of normalized expression of CD11b and podoplanin in PDL1+ macrophages from residual (n=47,605) and primary HCC (n=6108) (both pAdj value <3.0x10⁻³⁰⁰).
- h. Comparison of normalized expression of PD1 and TIM3 in T cells and NK cells from residual (T cells, n=16,549; NK cells n= 11,701) and primary HCC (T cells, n=45,494; NK cells n=2111)(both pAdj value <3.0x10⁻³⁰⁰).

Statistical significance was assessed by unpaired, two-tailed t-test, Benjamini-Hochberg (BH) adjustment was used for p values.

Abbreviations: HCC- hepatocellular carcinoma, H&E- hematoxylin and eosin, CODEX- co-detection by indexing, DAPI- 4',6-diamidino-2-phenylindole, CD- cluster of differentiation, PanCK- pan cytokeratin, aSMA-smooth muscle alpha actin, PDL1- programmed death ligand 1, BCL2- B-cell lymphoma 2, PD1- programmed cell death protein 1, TIM3- T cell immunoglobulin and mucin domain-containing protein 3, Exh-Exhausted, NK-natural killer, Sig- significant.

FIGURE 3 Remodeling of Spatial Interactions Between Tumor and Immune Cells in Residual HCC



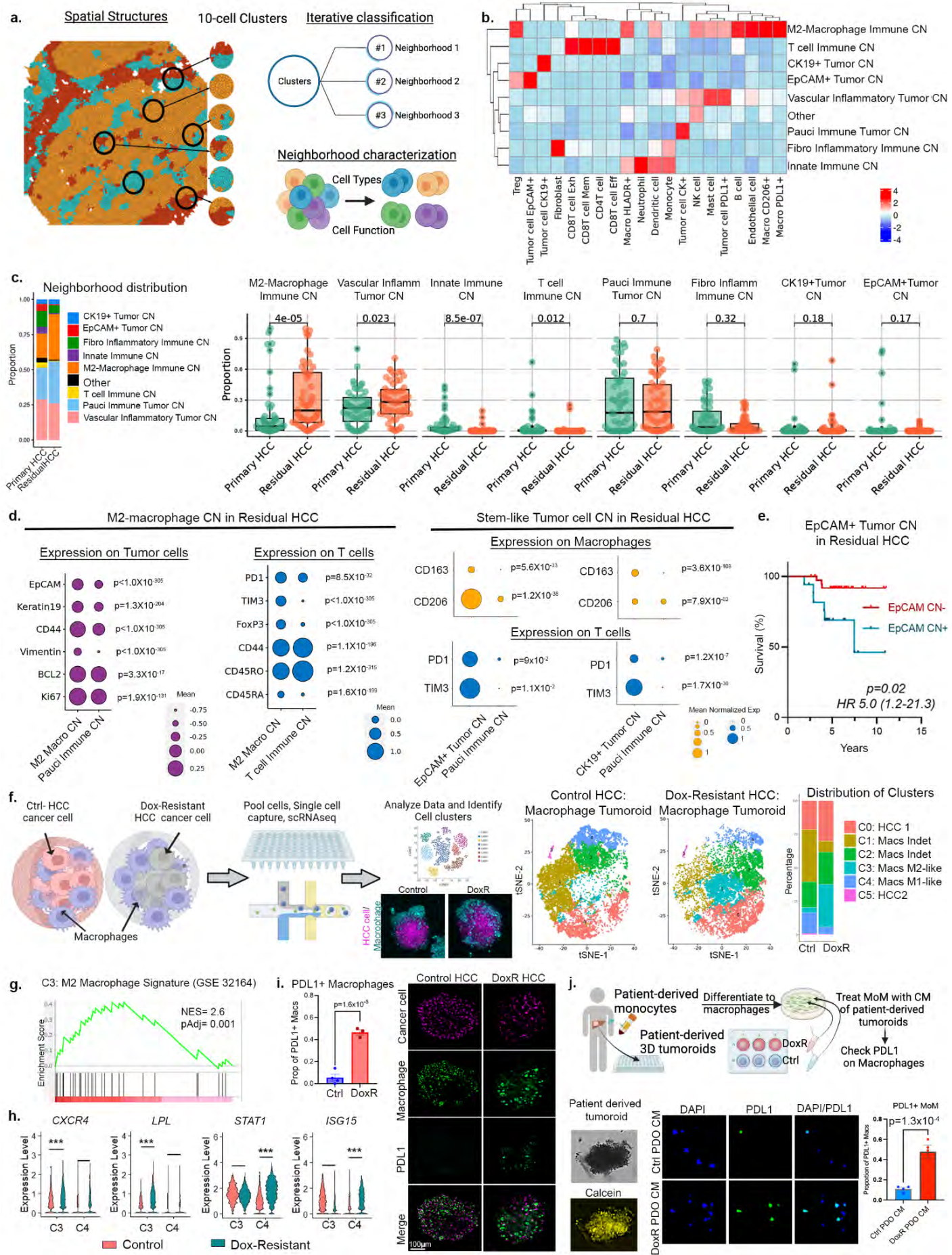
- Alluvial plot of tumor cell subtype and immune cell interactions in residual (n=55) and primary HCCs (n=53). Height of each unit is proportional to the frequency of interaction between two cell types. Only significant interactions with $p_{Adj} < 0.05$ are depicted.
- Size-modulated circular heatmap showing mean frequency and adjusted p values of direct interactions between tumor cell subtypes and PDL1+ macrophages in residual (n=55) and primary HCCs (n=53).
- Size-modulated circular heatmap showing mean frequency and adjusted p values of direct interactions between tumor cell subtypes and exhausted CD8T cells in residual (n=55) and primary HCCs (n=53).

- d. Kaplan Meier plots signifying the recurrence-free survival of tumors stratified by median frequency of interaction between EPCAM+ tumor cells and either CD206+ or PDL1+ macrophages in residual HCC (n=55). CODEX representative IF images demonstrate the interaction between representative cells. Log rank test used to statistically compare the groups.
- e. CODEX imaging representations of PDL1+ macrophage interactions with exhausted and effector CD8+ T cells, shown with box plots quantifying the proportion of interactions in primary (n=53) compared to residual HCC (n=55).
- f. CODEX imaging representations of PDL1+ macrophage interactions with fibroblasts and endothelial cells, shown with bar plots quantifying the proportion of interactions in primary (n=53) compared to residual HCC (n=55).
- g. Model of direct and indirect interactions with a single central cell using the scalar variable “cell-cell distance”. R² values for predicting Ki67 and BCL2 marker expression in radius of increasing sizes. Volcano plots show that increasing neighborhood sizes explain more variance in expression of a central cell’s Ki67 and BCL2. R² values for Ki67 are higher on average for a neighborhood radius of 100µm vs a neighborhood radius of 25µm (Wilcoxon rank sums pAdj-value 8.48×10^{-6}), and for BCL2 (Wilcoxon rank sums pAdj-value 1.76×10^{-5}).
- h. Size-modulated circular heatmap showing mean frequency and adjusted p values of indirect interactions between tumor cell subtypes and PDL1+ macrophages in residual (n=55) and primary HCCs (n=53).
- i. Size-modulated circular heatmap showing mean frequency and adjusted p values of frequency of indirect interactions between tumor cell subtypes and exhausted CD8T cells in residual (n=55) and primary HCCs (n=53).

Statistical significance was assessed by unpaired, two-tailed t-test, Benjamini-Hochberg (BH) adjustment was used for p values.

Abbreviations: H&E- hematoxylin and eosin, CODEX- co-detection by indexing, HCC- hepatocellular carcinoma, DAPI- 4',6-diamidino-2-phenylindole, CD- cluster of differentiation, PanCK- pan cytokeratin, CK19- cytokeratin 19, EPCAM- epithelial cell adhesion molecule, aSMA-smooth muscle alpha actin, PDL1- programmed death ligand 1, BCL2- B-cell lymphoma 2, PD1- programmed cell death protein 1, TIM3- T cell immunoglobulin and mucin domain-containing protein 3, HLA-DR- Human Leukocyte Antigen – DR isotype, Treg-regulatory T cell, NK-natural killer, Exh-exhausted, Eff- effector, NK - natural killer

FIGURE 4 Synchronized Spatial Remodeling of Neighborhood Structures in Residual HCC



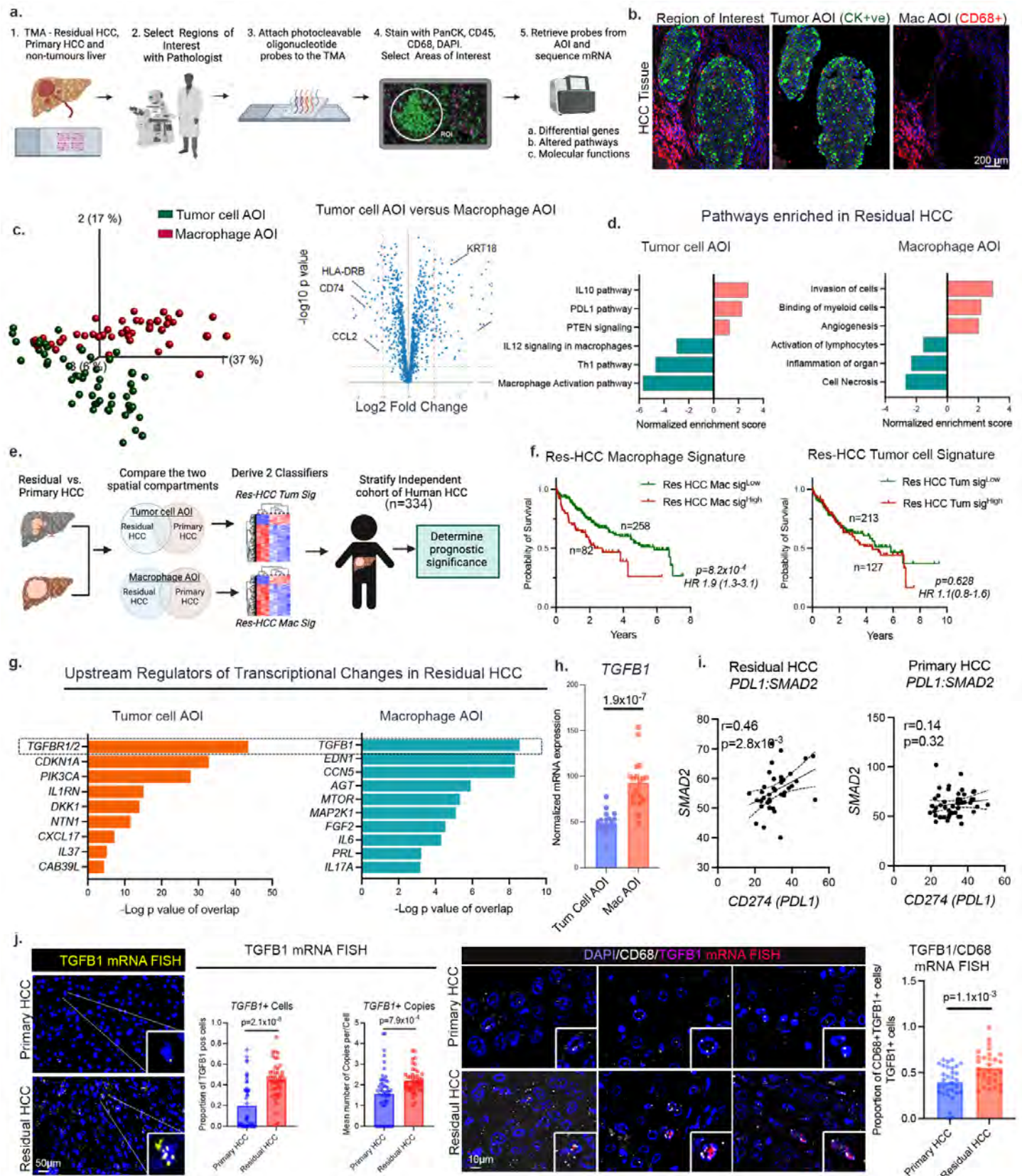
- a. Schematic showing cellular neighborhood (CN) identification based on an iterative 10-cell clustering algorithm. Color codes show hypothetical spatial structures within the tumor microenvironment.
- b. Heatmap demonstrating the cellular compositions of the nine cellular neighborhoods defined in this study.
- c. Comparison of tumor and immune cell neighborhood distributions in primary (n=53) and residual HCCs (n=55). Box plots comparing the proportion of eight cellular neighborhoods in primary (n=53) and residual HCCs (n=55).
- d. Size-modulated circular heatmap showing mean expression of markers on y-axis in tumor cells and T cells in residual HCC within the M2-macrophage CN (tumor cells, n= 17046; T cells, n=4299) compared to the pauci-immune tumor CN (tumor cells, n= 109, 391) or T cell immune CN (T cells, n= 8345) respectively, adjusted p values shown next to the plot. Size-modulated circular heatmap showing mean expression of markers on y-axis on macrophages and T cells within the EpCAM+ tumor cell CN (macrophages=272, n= 17046; T cells, n=13) and CK19+ tumor cell CNs (macrophages, n= 1201; T cells, n=354) compared to the pauci-immune tumor CN (macrophages, n= 4401; T cells, n=239) respectively, adjusted p values shown next to the plot.
- e. Kaplan-Meier plot showing recurrence-free survival in patients with tumors stratified based on the presence (n=12) or absence (n=43) of EPCAM+ tumor cell CN in residual HCC (n=55). Log rank test used to statistically compare the groups.
- f. Schematic of in vitro 3D tumoroid co-culture of control and doxorubicin-resistant Huh7 HCC cell lines with THP1 macrophages followed by single-cell RNA sequencing followed by cell clustering and quantification.
- g. Characterizing the macrophage C3 and C4 between doxorubicin-resistant (DoxR) and control samples. Gene set expression analysis shows enrichment of the M2-like macrophage signature in the C3 cluster of macrophages enriched in the DoxR samples.
- h. Volcano plot shows mean expression of key differentially expressed genes in C3 versus C4 clusters.
- i. Quantification of PDL1+ macrophages by immunofluorescence in 3D heterotypic tumoroids of control or doxorubicin-resistant (DoxR) Huh7 cancer cells with THP1 macrophages.
- j. Schematic of *in vitro* assay using primary HCC patient-derived 3D tumoroids and monocyte-derived macrophages from patients with HCC. Calcein staining demonstrates viability of 3D patient derived tumoroids. PDL1 expression in monocyte-derived macrophages treated with conditioned media from doxorubicin resistant patient-derived tumoroid (n=4) versus control (n=4). Unpaired t-tests used to compare the proportion of PDL1+ macrophages between the two groups.

Statistical significance was assessed by unpaired, two-tailed t-test, Benjamini-Hochberg (BH) adjustment was used for p values.

Abbreviations: H&E- hematoxylin and eosin, CODEX- co-detection by indexing, HCC- hepatocellular carcinoma, DAPI- 4',6-diamidino-2-phenylindole, CN-cellular neighborhood, CD- cluster of differentiation, PanCK- pan cytokeratin, CK19- cytokeratin 19, EPCAM- epithelial cell adhesion molecule, aSMA-smooth muscle alpha actin, PDL1- programmed death ligand 1, BCL2- B-cell lymphoma 2, PD1- programmed cell death protein 1, TIM3- T cell immunoglobulin and mucin domain-containing protein 3, HLA-DR- Human Leukocyte Antigen – DR isotype, Treg-regulatory T cell, NK-natural killer, Mem-memory, Exh-exhausted.

*** $p<0.001$.

FIGURE 5 TGF β pathway activation promotes persistence of residual tumor cells in HCC

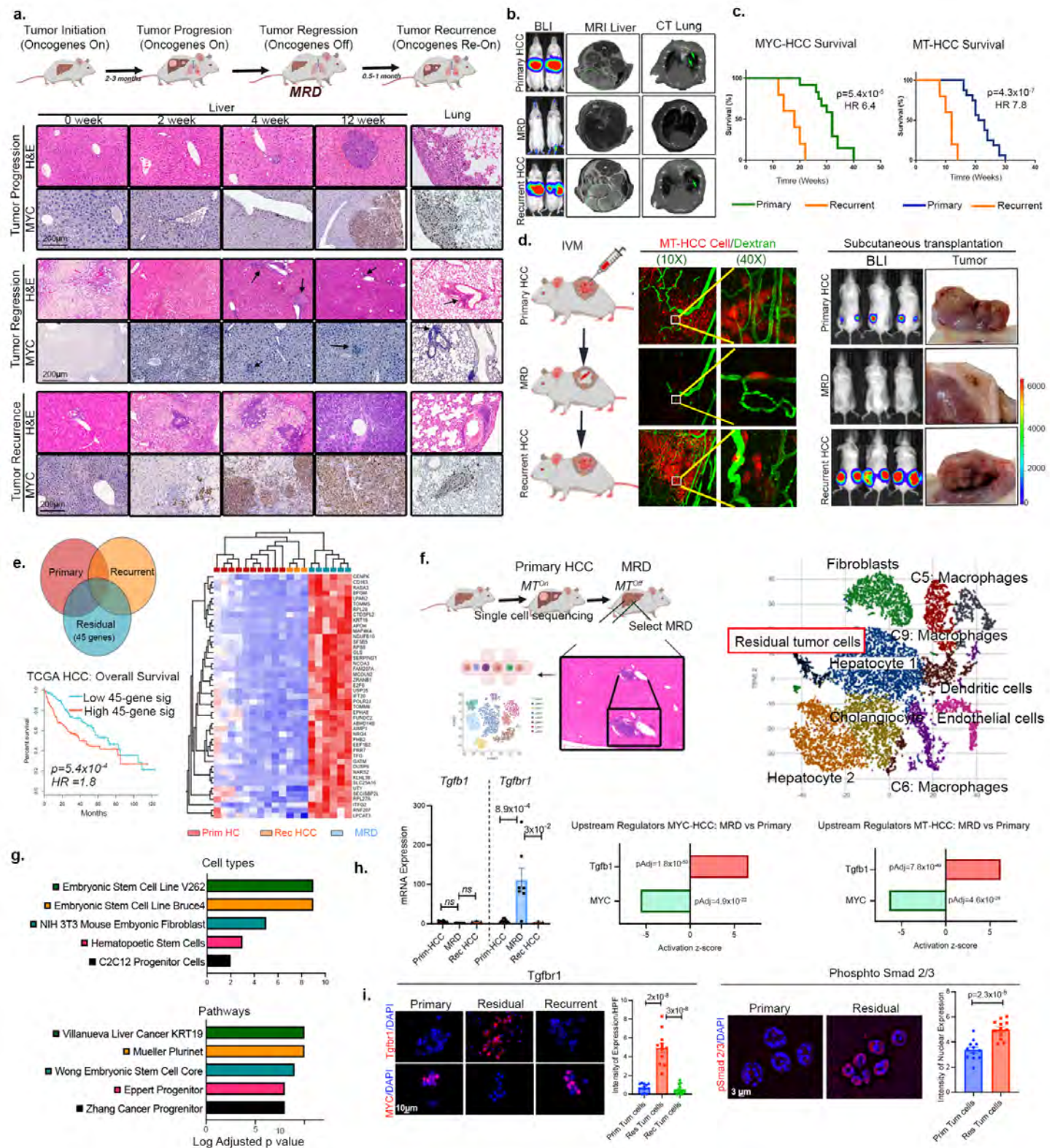


- a. Workflow of Nanostring spatial transcriptomics analysis. The expression of targeted transcriptomes of cancer and immune-related genes were quantified in tumor cell and macrophage areas of interest (AOI).

- b. Representative immunofluorescent regions of interest (ROI) showing tumor cell and macrophage-enriched areas of interest (AOI) based on the expression of panCK, CD45, CD68, DAPI.
- c. Principal Component Analysis (PCA) and volcano plot showing differential expression of genes in the tumor cell (n=53) and macrophage (n=52) AOIs.
- d. Molecular pathways activated in tumor cells (n=19 vs. n=11) and macrophage AOIs (n=18 vs. n=9) of residual HCC compared to non-tumorous liver samples.
- e. Schematic showing derivation of tumor cell and macrophage signatures from the spatial transcriptome data of primary and residual HCC.
- f. Kaplan-Meier curve showing the prognostic significance of tumor cell and macrophage signatures applied to a validation cohort of human HCC (n=334). Log rank test used to compare the groups.
- g. Upstream regulators of transcriptional regulators of gene expression changes in the tumor cell and macrophage AOIs of residual HCC compared to non-tumorous liver samples.
- h. Plot comparing *TGFB1* gene expression levels in tumor cells (n=19) and macrophage AOIs (n=18) of residual HC.
- i. Correlation plot showing co-expression of *SMAD2* and *CD274 (PDL1)* in residual HCC (n=38) but not primary HCC (n=48). Spearman test to correlate expression.
- j. Representative fluorescent mRNA FISH images along with quantification of *TGFB1* mRNA expression in primary (n=51) and residual HCC (n=46). Representative fluorescent mRNA FISH images along with quantification of *TGFB1* and *CD68* mRNA expression in primary (n=31) and residual HCC (n=30).

Abbreviations: DAPI- 4',6-diamidino-2-phenylindole, TMA-tumor microarray, AOI- area of interest, CODEX-co-detection by indexing, rHCC- residual hepatocellular carcinoma, TGFB1- transcription growth factor beta 1

FIGURE 6 Transgenic mouse model of HCC demonstrates recurrence of HCC can arise from MRD

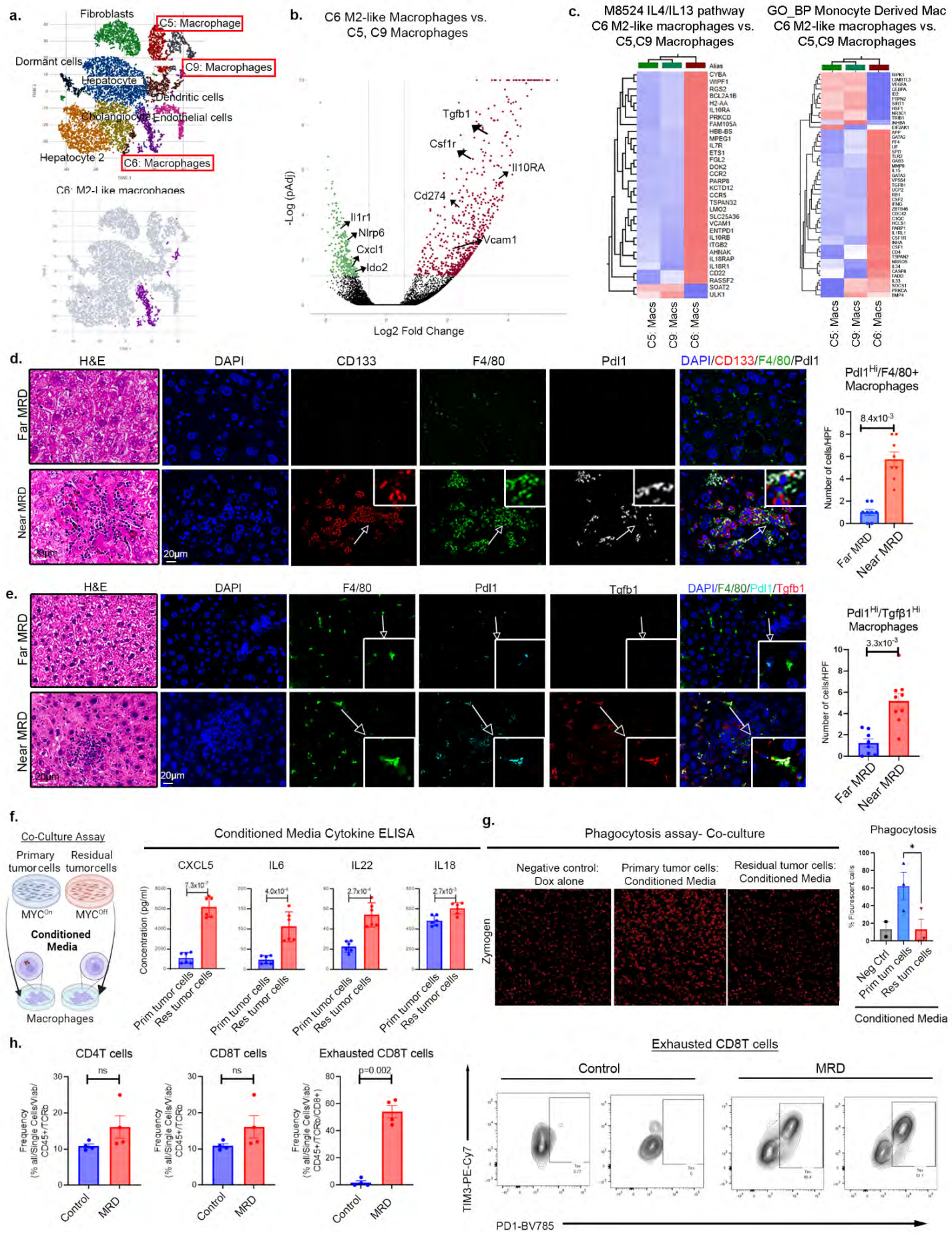


- Schematic illustrates the process of oncogene activation triggering tumor progression, subsequent inactivation leading to tumor regression, and then re-activation promoting recurrence. Representative H&E and IHC for MYC show the temporal evolution of tumor progression and tumor regression in MYC/Twist1 HCC in the liver and lungs.
- Representative bioluminescence imaging, MRI liver, and CT lungs show regression of tumors upon oncogene inactivation and recurrence upon oncogene reactivation. MRD-bearing mice do not show any radiological evidence of tumor.

- c. Overall survival of MYC-HCC (n=17) and MT-HCC (n=21) mice with primary tumor from oncogene activation (MYC-HCC=12, MT-HCC=16) or with recurrent tumor from oncogene reactivation in MRD-bearing mice (MYC-HCC=5, MT-HCC=5). Log rank test used to compare the survival in the Kaplan-Meier analysis.
- d. Intravital microscopy (MYC-HCC n=3, MT-HCC n=3) and subcutaneous transplant allograft model (MYC-HCC n=10, MT-HCC n=10) confirms persistence of a small proportion of viable residual tumor cells in perivascular niches and serves as a source of recurrence upon oncogene reactivation.
- e. Cross-species transcriptome analysis of a 45-gene signature enriched in residual murine HCC (n=6) and not primary (n=10) or recurrent HCC (n=3) was able to predict survival in an independent human HCC cohort (n=372) patients. Log rank test used to compare survival between Kaplan Meier curves.
- f. Experimental scheme for single-cell RNA sequencing of microdissected areas containing *in vivo* MRD. Graph-based clustering of single-cell RNA sequencing represented as UMAP with each color representing the correspondingly named cell type (n=15,300 cells). The residual tumor cells are highlighted in a red box.
- g. Overlap with cell types and enriched pathways in residual tumor cells compared to hepatocyte clusters in residual tumor cells in scRNAseq of MRD.
- h. Expression of *Tgfb1* and *Tgfbr1* in primary (MYC-HCC=5, MT-HCC=5), residual HCC (MYC-HCC=3, MT-HCC=3) and recurrent HCC (MYC-HCC=3). Unpaired t test used to compare the mean between the groups. Horizontal bar plot showing activation of Tgfb1 pathway as upstream regulator of transcriptional changes in MYC- and MT-HCC MRD upon MYC pathway inactivation in MRD.
- i. Expression of Tgfbr1 by IF staining of primary cancer cell lines derived from MYC-HCC upon MYC inactivation and reactivation. Representative IF images and quantification of phosphorylation of smad2/3 primary cancer cell lines derived from MYC-HCC upon MYC inactivation. Mean and SEM are shown (n=12 each). Unpaired t test used to compare the mean between the groups.

Abbreviations: HCC- hepatocellular carcinoma, CT- computed tomography, IHC- immunohistochemistry, IF-immunofluorescence, TGFB- transforming growth factor beta, H&E-hematoxylin and eosin, MRI- magnetic resonance imaging, BLI-bioluminescence imaging, IVM-intravital microscopy, Prim-primary, Res-residual, Rec-recurrent, MRD- Minimal residual disease, HR-hazard ratio

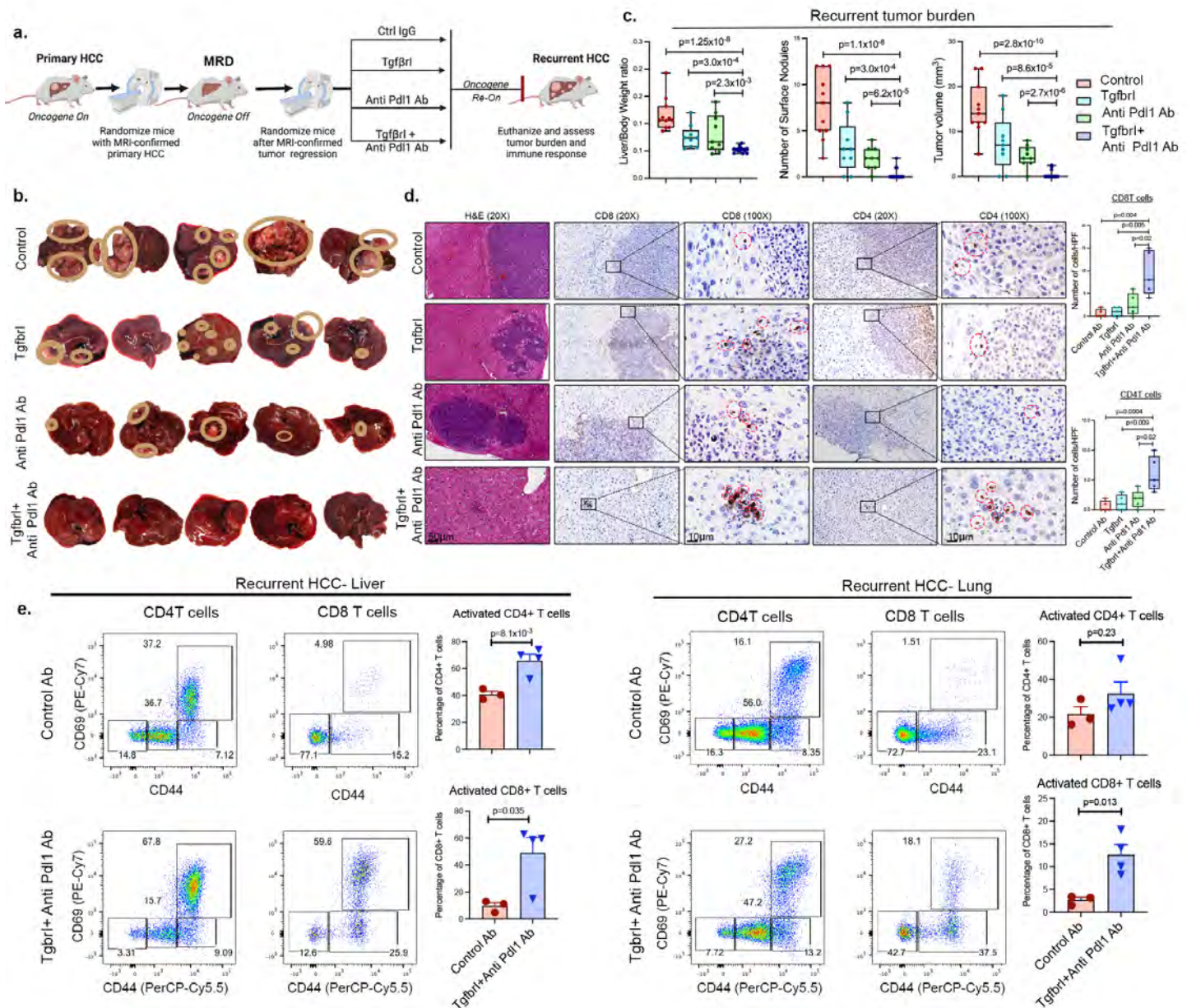
Figure 7 Mechanisms of Immune Evasion by Cancer Stem Cells in the MRD niche



- a. Graph based clustering of single-cell RNA sequencing of MRD represented as UMAP with each color representing the correspondingly named cell type (n=15,300 cells). The three subsets of macrophages are highlighted in a red box. The M2-like macrophage cluster (C6) is shown separately in the UMAP below.
- b. Volcano plot showing the differentially expressed genes between the M2-like C6 cluster of macrophages and the C5 and C9 cluster of M1-like macrophages ($p\text{Adj}<0.05$) are shown in green if underexpressed or red if overexpressed in M2-like macrophage cluster.
- c. Heatmap showing the enrichment of gene signature of M2-like macrophage polarization and monocyte-derived macrophage differentiation in the M2-like C6 cluster of macrophages than the C5 and C9 cluster of M1-like macrophages.
- d. Representative H&E and immunofluorescence images of CD133+ stem-like cancer cells and Pdl1+ macrophages near MRD (<200 μm) compared to liver distant from MRD. Bar plot shows comparison for mean PDL1+ macrophages between groups using unpaired T-tests (n=8 each group).
- e. Representative H&E and immunofluorescence images of Tgf β 1 expression on Pdl1+ macrophages near MRD (<200 μm) compared to liver distant from MRD. Bar plot shows comparison for mean Tgf β 1+/PDL1+ macrophages between groups using unpaired T-tests (n=9 each group).
- f. Schematic showing collection of conditioned media from primary or residual HCC cells from MYC-HCC to treat macrophages *in vitro*. Bar plot shows comparison for mean concentration of cytokines secreted by residual tumor cells (n=6) and primary tumor cells (n=6) using unpaired t-tests.
- g. Macrophages are treated with conditioned media from negative control (n=2) primary (n=3) or residual tumor cells (n=3) *in vitro*. Bar plot shows comparison for phagocytosis between groups using unpaired T-tests.
- h. Bar plots showing comparison of mean CD4T, CD8T, and exhausted CD8T cells in livers with MRD (n=4) versus control non-MRD livers (n=4) using unpaired t-tests. Representative flow cytometry plots of exhausted CD8T cells based on TIM3 and PD1 expression.

Abbreviations: HCC- hepatocellular carcinoma, TGFB -transforming growth factor beta, H&E-hematoxylin and eosin, Ctrl-control, Res-residual, MRD- Minimal residual disease.

FIGURE 8 Combined blockade of Tgf β r1 and Pdl1 prevents recurrence from MRD in transgenic MYC-driven HCC

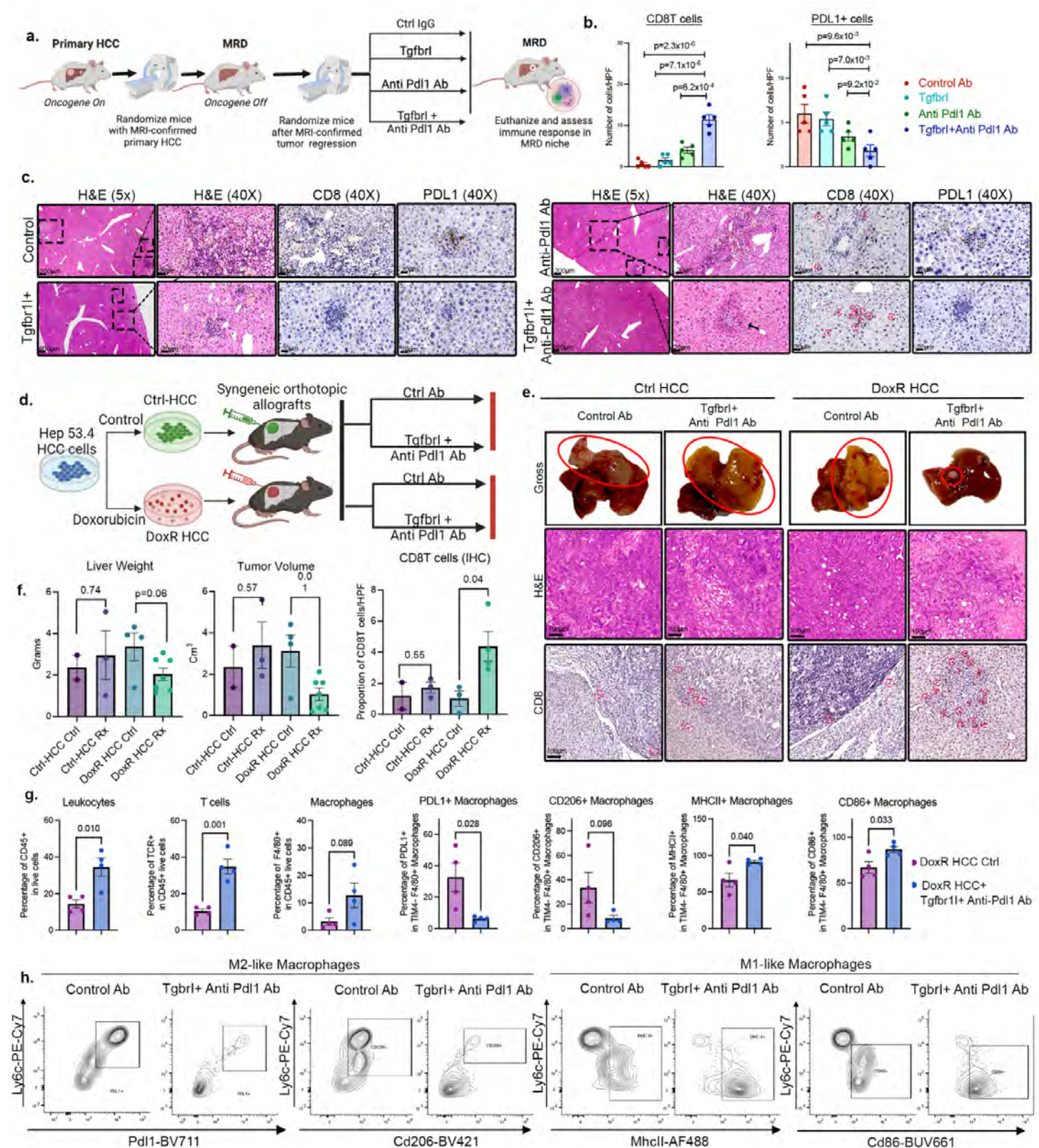


- Experimental scheme for treatment of oncogene-deprived MRD-bearing mice with control antibody or monotherapy with Tgfbr inhibitor (Tgfbr1) or anti-Pdl1 or their combination. Treatment is followed by oncogene re-activation to induce tumor recurrence.
- Representative gross images of recurrent tumor burden upon oncogene re-activation in the liver of mice treated with control antibody or monotherapy with Tgfbr1 or anti-Pdl1 inhibitor or their combination.
- Quantification of recurrent tumor burden upon oncogene activation in the liver of MYC-HCC and MT-HCC mice treated with control antibody (n=11) or monotherapy with Tgfbr1 inhibitor (n= 9) or anti-Pdl1 inhibitor (n=9) or their combination (n=16). Box plots compare the mean between the groups with unpaired t-tests.
- Representative images and quantification from H&E staining and IHC staining for CD4 and CD8 in recurrent tumors in mice treated with control antibody (n=5) or monotherapy with Tgfbr1 (n=5) or anti-Pdl1 inhibitor (n=5) or their combination (n=5). Box plots compare the mean between the groups with unpaired t-tests.
- Representative flow cytometry images and quantification of activated CD4 and CD8T cells which are CD69+/CD44^{high} in the recurrent tumor in the liver and lungs of MYC-HCC and MYC/Twist1-HCC mice

treated with control antibody (n=3) or combination therapy with Tgfb1l and anti-Pdl1 inhibitor (n=4). Bar plots compare the mean between the groups with unpaired t-tests.

Abbreviations: HCC- hepatocellular carcinoma, TGFB -transforming growth factor beta, H&E-hematoxylin and eosin, Ctrl-control, Res-residual, MRD- Minimal residual disease.

FIGURE 9 Combined blockade of Tgf β r1 and Pd11 eliminates oncogene-deprived residual tumor cells and doxorubicin-resistant murine HCC.



- a. Experimental scheme for treatment of oncogene-deprived residual HCC-bearing mice with control antibody (n=5) or Tgfb1 (n=5) or Pd11 inhibitors (n=5) or combination therapy with Tgfb1 and anti-Pd11 inhibitor (n=5). Residual tumor niches are then evaluated for immune response.

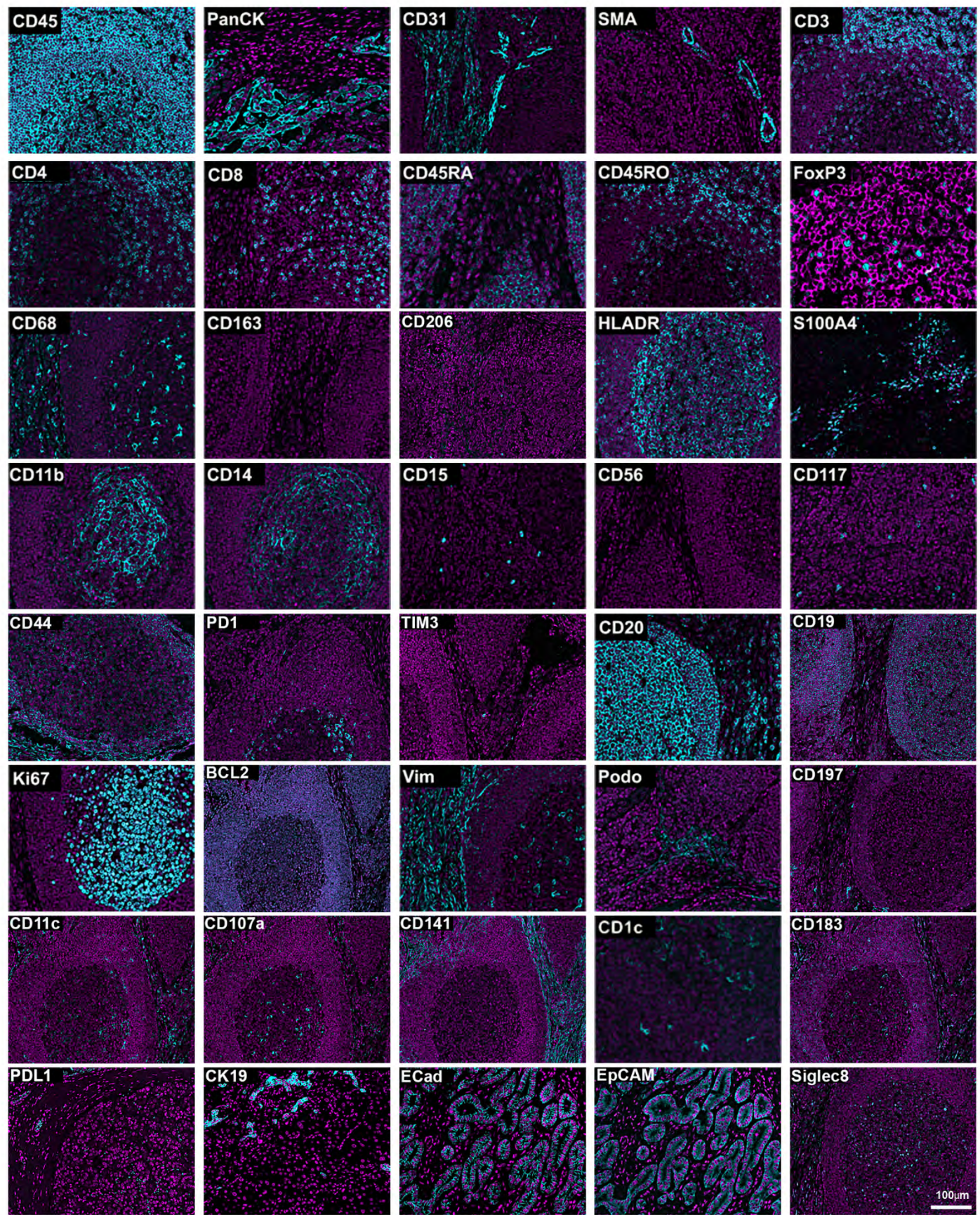
- b. Quantification of IHC staining for CD8 and PDL1 in residual HCC niche in mice treated with control antibody (n=5) or Tgfbr1 (n=5) or Pdl1 inhibitors (n=5) or combination therapy with Tgfbr1 and Pdl1 inhibitors (n=5). Bar plots compare the mean between the groups with unpaired t-tests.
- c. Representative H&E staining and IHC staining for CD8 and PDL1 in MRD (red arrows in gross image and black boxes in H&E) in mice treated with control antibody (n=5) or Tgfbr1 (n=5) or Pdl1 inhibitors (n=5) or combination therapy with Tgfbr1 and Pdl1 inhibitors (n=5).
- d. Schematic showing the establishment of mouse model of control (n=5) or doxorubicin-resistant syngeneic orthotopic allografts (n=11) which were then treated with control antibody (n=6) or combination therapy with Tgfbr1 and anti-Pdl1 inhibitor (n=10).
- e. Representative gross images, H&E and IHC images of control or doxorubicin-resistant orthotopic HCC-bearing mice treated with control antibody (n=6) or combination therapy with Tgfbr1 and anti-Pdl1 inhibitor (n=10). IHC for CD8T cells shows in the bottom panel.
- f. Quantification of tumor burden and CD8T cells in the liver of control or doxorubicin-resistant orthotopic HCC-bearing mice treated with control antibody (n=6) or combination therapy with Tgfbr1 and anti-Pdl1 inhibitor (n=10). Bar plots compare the mean between the groups with unpaired t-tests.
- g. Flow cytometry based quantification of tumor infiltrating leukocytes, T cells, M2-like (PDL1+ or CD206+) and M1-like macrophage (CD86+ or MHCII+) subsets in doxorubicin-resistant (n=8) orthotopic HCC-bearing mice treated with control antibody (n=4) or combination therapy with Tgfbr1 and anti-Pdl1 inhibitor (n=4). Bar plots compare the mean between the groups with unpaired t-tests.
- h. Representative flow cytometry images and quantification of M1-like and M2-like macrophages within the tumor in the doxorubicin-resistant orthotopic HCC-bearing mice treated with control antibody or combination therapy with Tgfbr1 and anti-Pdl1 inhibitor.

Abbreviations: HCC- hepatocellular carcinoma, Tgfb -transforming growth factor beta, H&E-hematoxylin and eosin, Ctrl-control, Res-residual, MRD- Minimal residual disease, DoxR- doxorubicin-resistant.

SUPPLEMENTARY FIGURES

Multi-omic Spatial Analysis Reveals Targetable Macrophage-Mediated Mechanisms of Immune Evasion in Hepatocellular Carcinoma Minimal Residual Disease

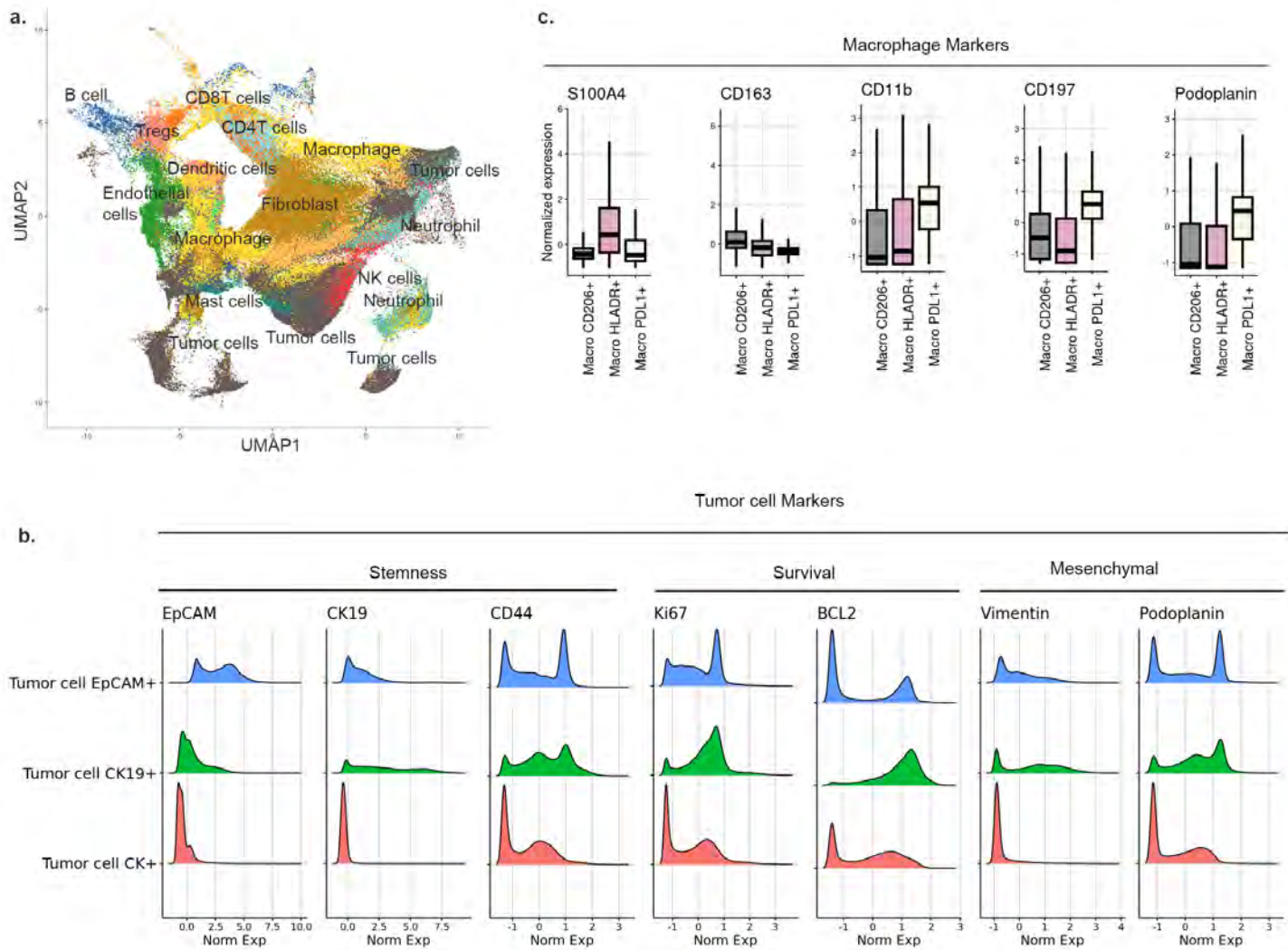
Supplementary Figure 1 CODEX Immunostaining of individual markers used in this study



Immunostained images containing each of the 41 tumor, immune, stromal, and function antibodies used in the multiplex CODEX assay. Magenta shows nuclei and teal color shows the respective markers showing in the box.

CD- cluster of differentiation, PanCK- pan cytokeratin, SMA-smooth muscle alpha actin, PDL1- programmed death ligand 1, FOXP3- Forkhead box P3 protein, HLA-DR - major histocompatibility complex II cell surface receptor, S100A4- S100 calcium binding protein A4, BCL2- B-cell lymphoma 2, PD1- programmed cell death protein 1, PDL1- programmed cell death ligand 1, TIM3- T cell immunoglobulin and mucin domain-containing protein 3, VIM- vimentin, Podo- Podoplanin, CK19- cytokeratin 19, ECad - e-cadherin, EPCAM- epithelial cell adhesion molecule, Siglec8 - sialic-acid binding immunoglobulin-like lectin.

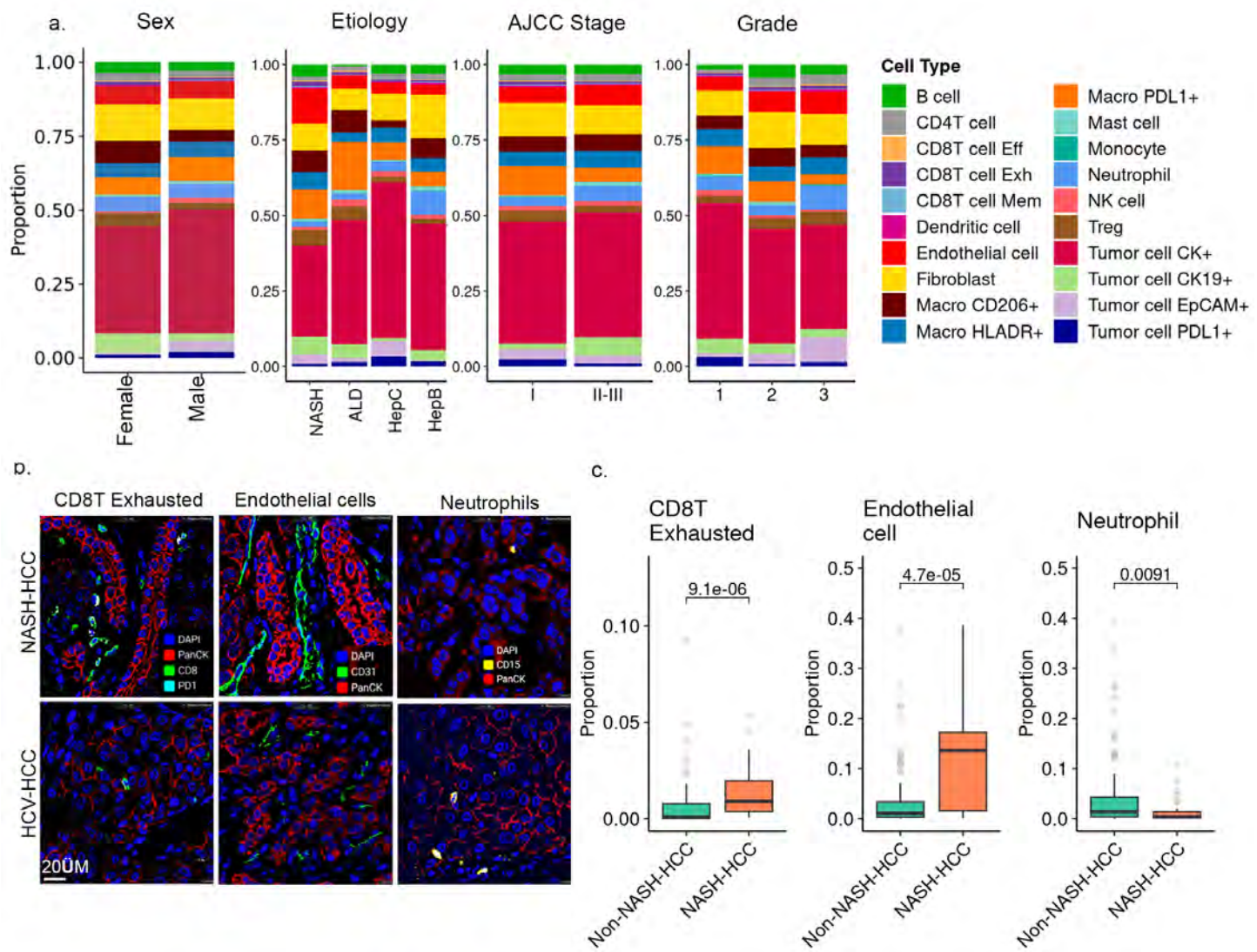
Supplementary Figure 2 identification and validation of major cell types using CODEX



- UMAP representation of 12 major cell subtypes identified by CODEX analysis of human HCC.
- Comparison of normalized expression patterns of stemness markers (EPCAM, CK19, CD44), survival markers (Ki67, BCL2), and mesenchymal markers (vimentin, podoplanin) between stem-like and non-stem-like tumor cell types identified by CODEX analysis of human HCCs.
- Comparison of normalized expression patterns of macrophage markers between three macrophage subsets identified by CODEX analysis of human HCCs.

Abbreviations: UMAP- uniform manifold approximation and projection for dimension reduction, CODEX- co-detection by indexing, HCC- hepatocellular carcinoma, CD- cluster of differentiation, CK- cytokeratin, EPCAM- epithelial cell adhesion molecule, BCL2- B-cell lymphoma 2

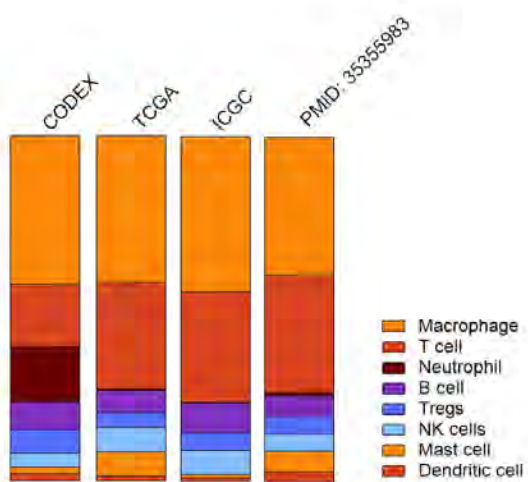
Supplementary Figure 3 Relative proportion of cells in clinical subtypes of HCC



- Stacked bar chart comparing relative proportions of all 20 immune and tumor cell subtypes identified by CODEX between self-reported sex (female, male), HCC etiologies (NASH, ALD, HepC, and HepB), AJCC Stage (I vs II-III), and grade (1, 2, and 3).
- CODEX image representations comparing exhausted CD8+ T cells, endothelial cell, and neutrophil presence in NASH-HCC compared to HCV-HCC
- Box plot comparisons of the proportions of exhausted CD8+ T cells, endothelial cells, and neutrophils in NASH vs non-NASH HCC.

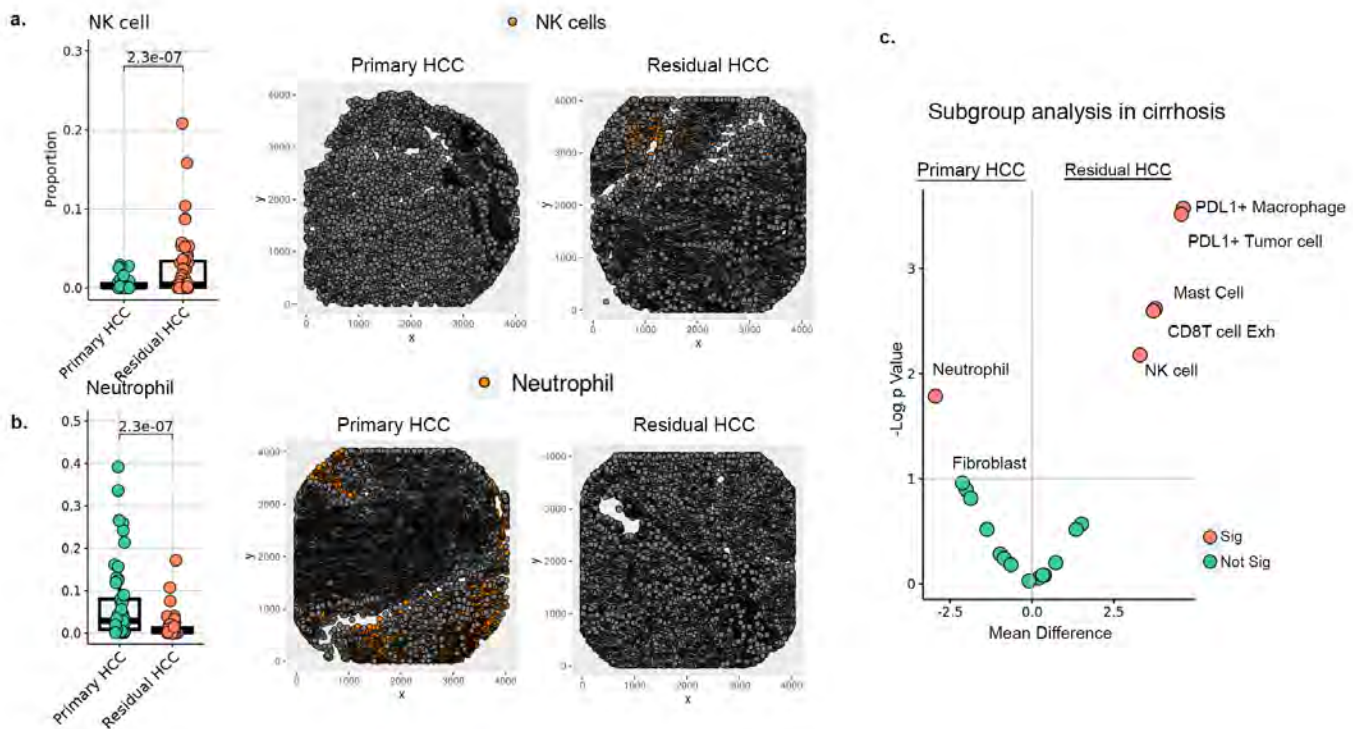
Abbreviations: CODEX- co-detection by indexing, HCC- hepatocellular carcinoma, NASH-nonalcoholic steatohepatitis, ALD- alcoholic liver disease, HepC- hepatitis C, HCV- hepatitis C virus, HepB- hepatitis B, CD- cluster of differentiation, HLA-DR - major histocompatibility complex II cell surface receptor, PDL1- programmed cell death ligand 1, DAPI- 4',6-diamidino-2-phenylindole, PanCK- pan cytokeratin

Supplementary Figure 4 Comparison of cell proportions in CODEX with other published reports



Stacked Bar graph containing relatively similar proportions of immune cell populations in HCC as reported by CODEX analysis in this study, the Cancer Genome Atlas Project, the ICGC project and a single cell RNA sequencing research study PMID 35355983.

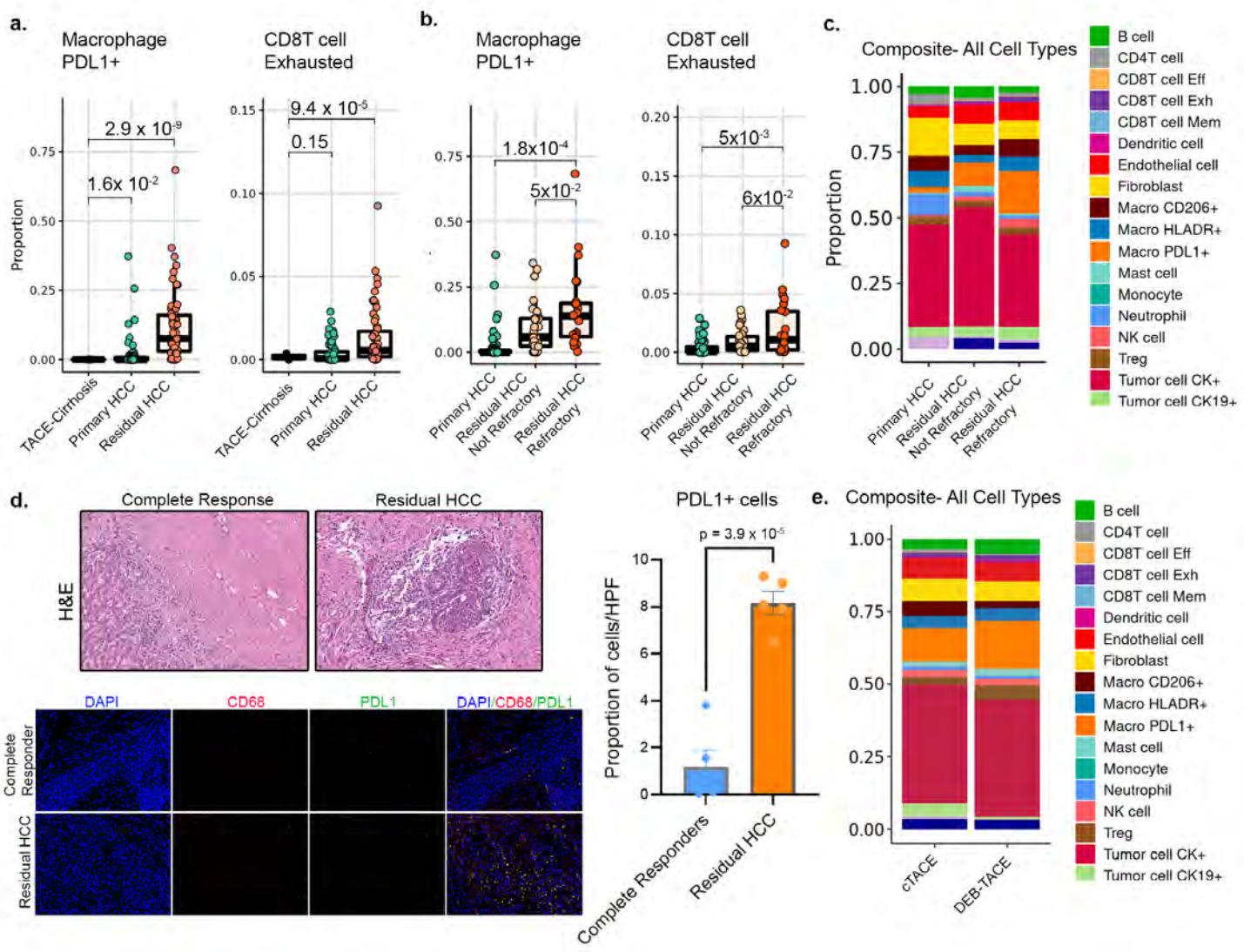
Supplementary Figure 5 Immune cell distribution in residual HCC



- Boxplot comparisons and Voronoi plot of representative cores of NK cell proportions in primary vs residual HCCs.
- Boxplot comparisons and Voronoi plot of representative cores of neutrophil proportions in primary vs residual HCCs.
- Volcano plot showing key tumor and immune cell populations (with statistical significance) in primary vs residual HCCs in the subgroup of HCCs arising in the cirrhotic liver.

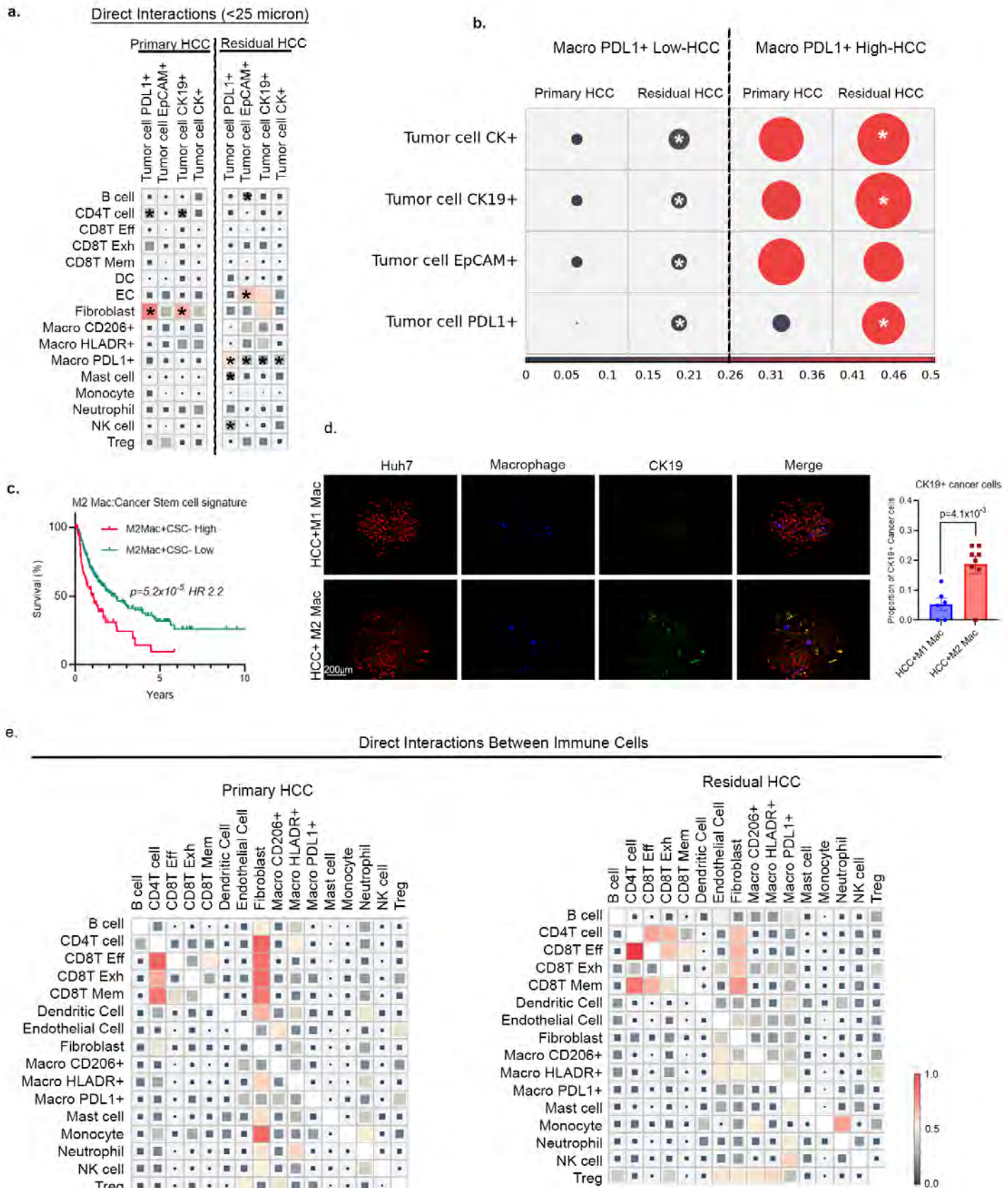
Abbreviations: HCC- hepatocellular carcinoma, NK- natural killer, CD- cluster of differentiation, PDL1- programmed cell death ligand 1

Supplementary Figure 6 Comparison of proportion of Immune cells based on response to TACE



- Boxplot comparisons of PDL1+ macrophages and exhausted CD8T cells between peritumoral TACE-exposed cirrhotic livers (n=3), primary (n=53) vs residual HCCs (n=55).
- Boxplot comparisons of PDL1+ macrophages and exhausted CD8T cells between primary (n=53), residual HCC- not refractory to TACE (n=21) vs residual HCC refractory to TACE (n=24).
- Stacked bar chart comparing relative proportions of all 20 immune and tumor cell subtypes identified by CODEX between primary (n=53), residual HCC- not refractory to TACE (n=21) vs residual HCC refractory to TACE (n=24).
- H&E and Immunofluorescence for PDL1+ macrophages in hepatic tissue with complete response to TACE (n=5) compared to residual HCC (n=5). Bar plots compare the proportion of PDL1+ cells between the two groups.
- Stacked bar chart comparing relative proportions of all 20 immune and tumor cell subtypes identified by CODEX between conventional TACE(cTACE, n=6) and doxorubicin-eluting beads TACE (DEB-TACE, n=49).

Supplementary Figure 7 Direct Interactions of tumor and immune cells in residual HCC

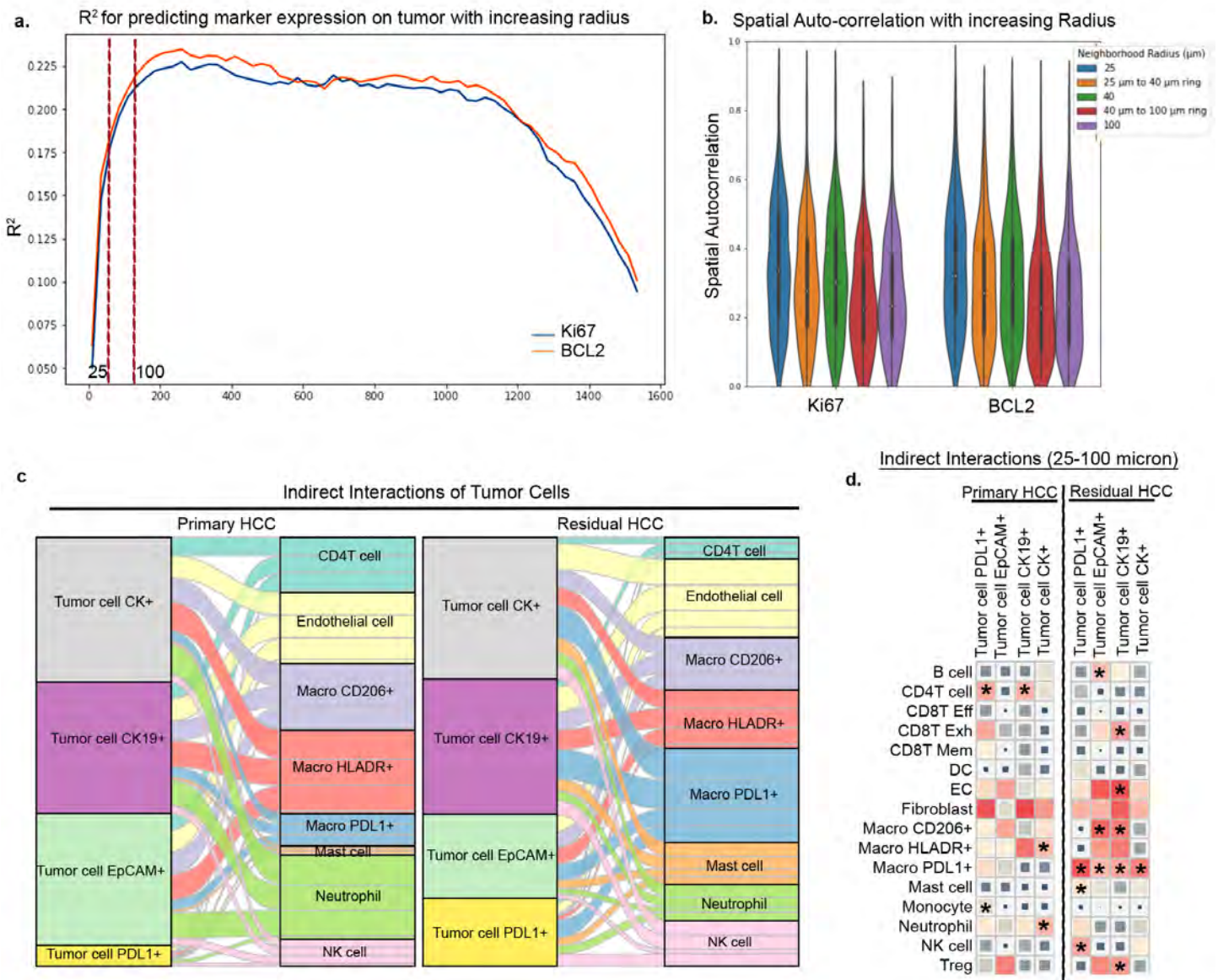


- a. Heatmap showing different patterns of direct interactions between the four tumor cell subtypes in primary (n=53) vs residual HCC (n=55). * indicated pAdj value<0.05.

- b. Dot plot showing mean frequency of interaction between tumor cell subtypes and PDL1+ macrophages in primary and residual HCC stratified by median frequency of PDL1+ macrophages in tumor. * indicated pAdj value<0.05.
- c. Kaplan Meir curve showing survival analysis of human HCC TCGA cohort (n=372) classified based on expression of genes related to M2-like macrophages and cancer stem cells.
- d. IF analysis of human HCC cell lines Huh7 co-cultured in 3D tumoroids with THP1 macrophages polarized to M1-like or M2-like macrophages. Bar plot shows quantification of CK19 expression on the 3D tumoroids.
- e. Heatmap of direct interactions between immune cells identified by CODEX in primary (n=53) and residual HCC (n=55).

Abbreviations: CODEX- co-detection by indexing, BCL2- B-cell lymphoma 2, CD- cluster of differentiation, CK- cytokeratin, EPCAM- epithelial cell adhesion molecule, PDL1- programmed cell death ligand 1, HLA-DR - major histocompatibility complex II cell surface receptor, NK- natural killer, TCGA- the cancer genome atlas project, HCC- hepatocellular carcinoma, M1- Type 1 Macrophage, M2- Type 2 Macrophage

Supplementary Figure 8 Indirect Interactions of tumor and immune cells in residual HCC

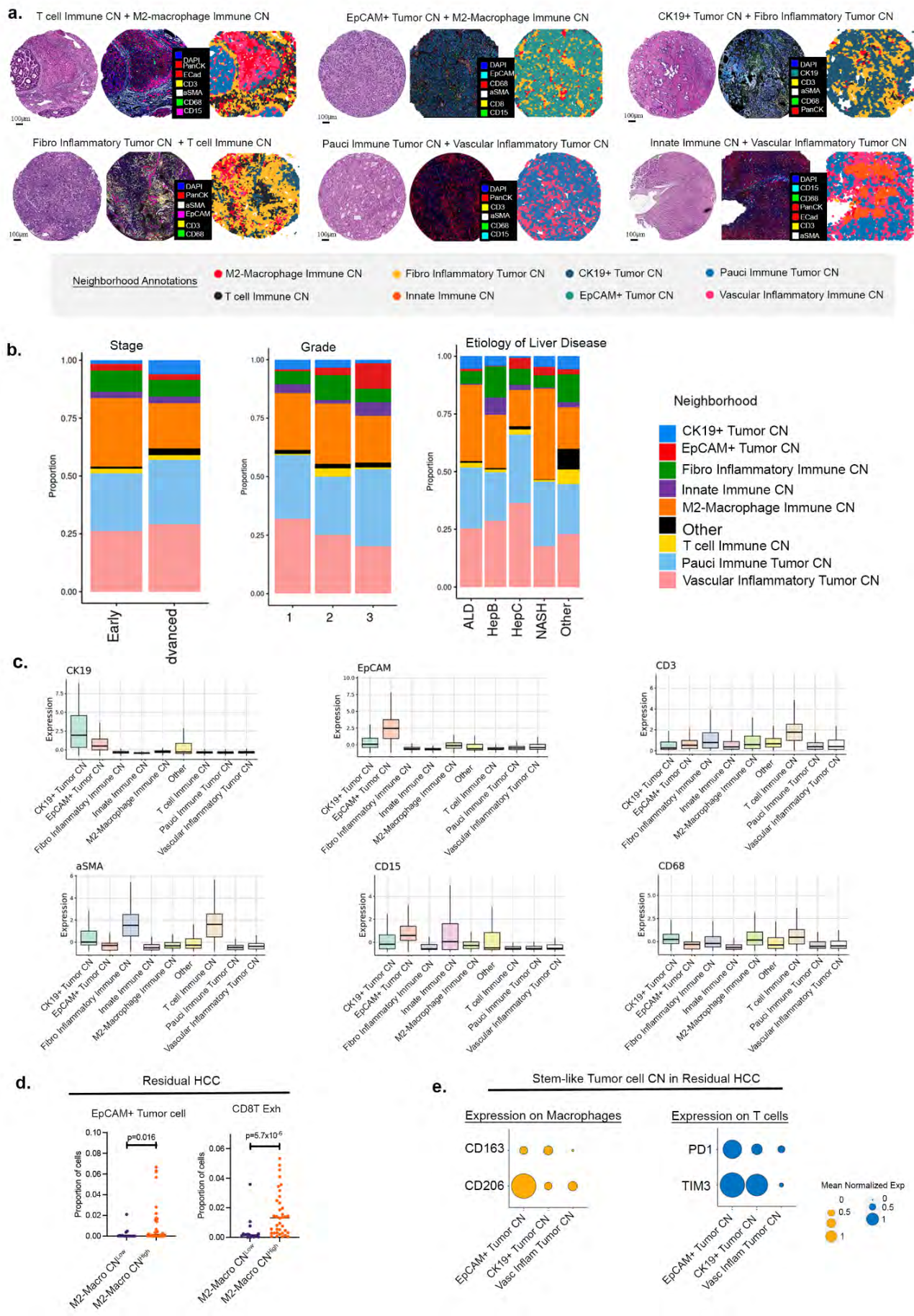


- R² values for predicting Ki67 and BCL2 marker expression in various cell types in radius of increasing sizes. Plotted lines are the R² values at each radius step averaged for all tumor regions. Within each region, linear regression models are fit to predict the expression of a marker, within a specific cell type.
- Large neighborhood sizes demonstrate reduced, but still significant spatial autocorrelation for Ki67 and BCL2 markers. Spatial autocorrelation is calculated using Geary's C statistic. The spatial autocorrelation for each marker is calculated independently for all tumor regions and reported as C' = 1 - C. The maximal spatial autocorrelation possible is 1.
- Alluvial plot of statistically significant indirect tumor cell subtype-immune cell interactions in primary (n=53) vs residual HCCs (n=55).
- Heatmap showing different patterns of indirect (25-100μm) interactions of tumor cell subtypes with immune cells in primary vs residual HCC. * indicated pAdj value<0.05.

Abbreviations: BCL2- *B-cell lymphoma 2*, HCC- *hepatocellular carcinoma*, Macro- *macrophages*, CK- *cytokeratin*, CD- *cluster of differentiation*, EPICAM- *epithelial cell adhesion molecule*, PDL1-

programmed cell death ligand 1, HLA-DR - major histocompatibility complex II cell receptor, NK-natural killer, HR- hazard ratio.

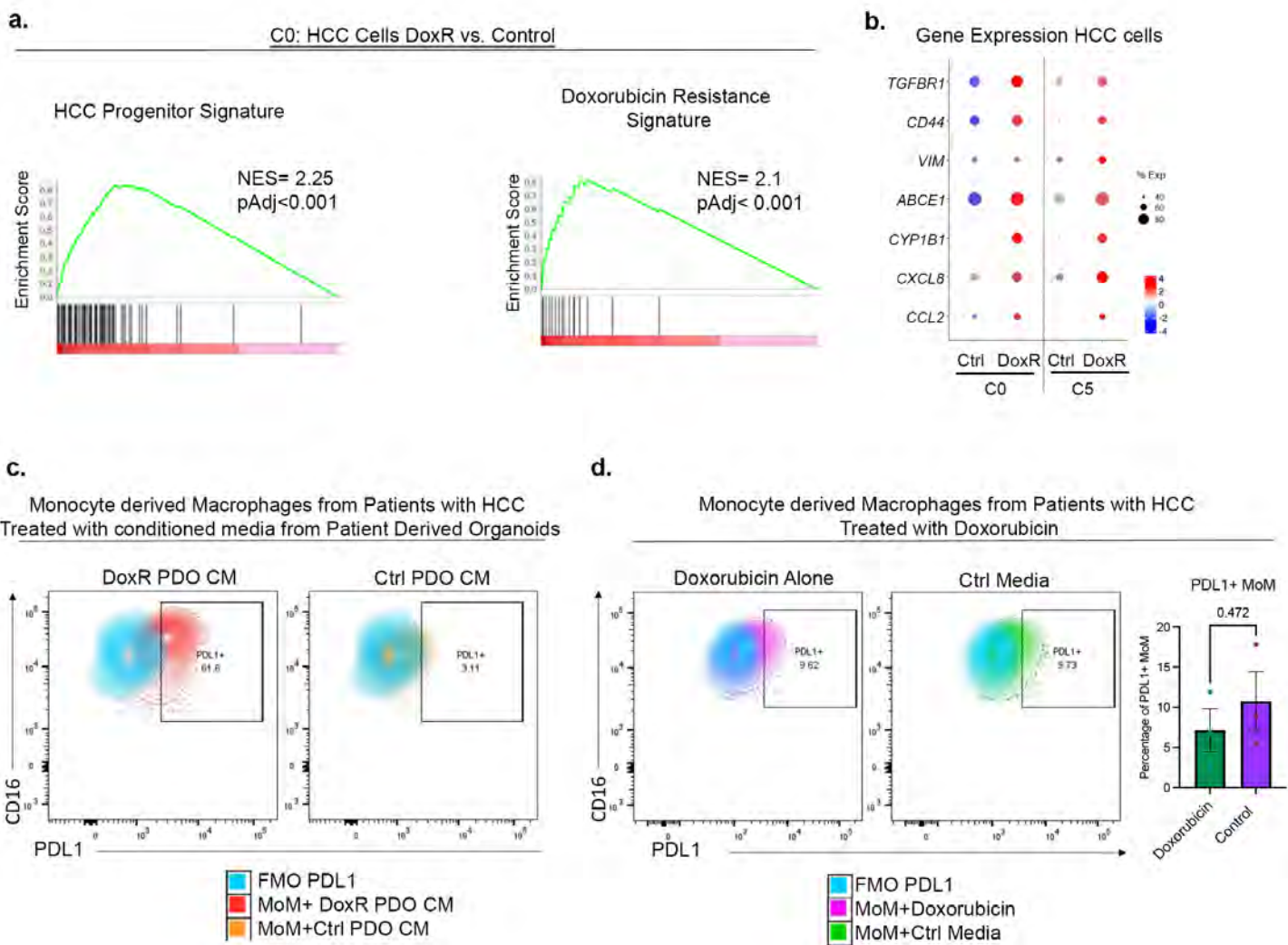
Supplementary Figure 9 Cellular neighborhood analysis of residual HCC



- a. Cross-matching of Voronoi plots showing spatial neighborhoods and the associated H&E and CODEX immunofluorescence staining images representations of the same tumor core. The canonical markers of key cells represented in each neighborhood are shown.
- b. Stacked bar chart comparing relative proportions of all 9 cellular neighborhoods identified by CODEX by HCC clinical Stage (early vs advanced), grade (1, 2, and 3), and etiology (NASH, ALD, HepC, and Hep B).
- c. Boxplot comparisons of CK19, EpCAM, CD3, aSMA, CD15, and CD68 expression amongst the identified cellular neighborhoods.
- d. Comparison of proportion of EpCAM+ tumor cells and exhausted CD8T cells in residual HCC stratified by median frequency of M2-macrophage CN.
- e. Comparison of specific canonical marker expression on macrophage and T cells in the EpCAM+ tumor CN, CK19+ tumor CN compared to vascular inflammatory tumor CN in residual HCC.

Abbreviations: HCC- hepatocellular carcinoma, CODEX- co-detection by indexin, Macro-macrophages, CK- cytokeratin, CD- cluster of differentiation, EPCAM- epithelial cell adhesion molecule, PDL1- programmed cell death ligand 1, aSMA- alpha smooth muscle actin, HLA-DR - major histocompatibility complex II cell surface receptor, BCL2- B-cell lymphoma 2, PD1- programmed cell death protein 1, PDL1- programmed cell death ligand 1, TIM3- T cell immunoglobulin and mucin domain-containing protein 3, FOXP3- Forkhead box P3 protein, NASH-nonalcoholic steatohepatitis, ALD- alcoholic liver disease, HepC- hepatitis C, HCV- hepatitis C virus, HepB- hepatitis B, CN- Cellular neighborhood

Supplementary Figure 10 Doxorubicin resistant residual HCC cells interaction with Macrophages



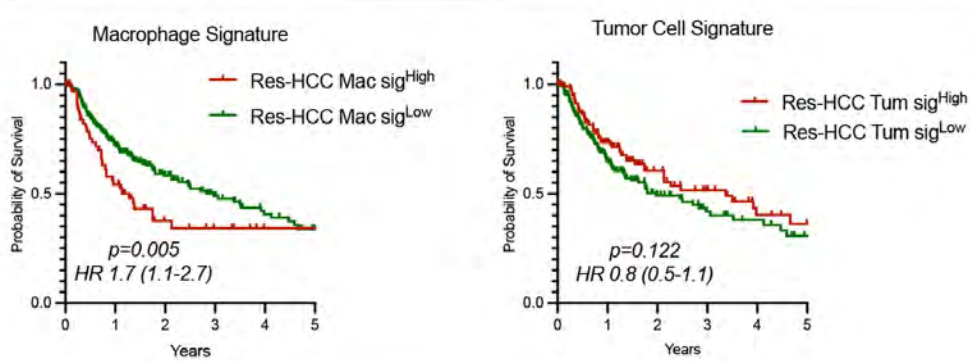
- Characterizing the HCC cancer cell clusters C0 and C5 between doxorubicin-resistant (DoxR) and control samples. Gene set expression analysis shows enrichment of HCC progenitor signature and doxorubicin resistance signature in the cancer cells in the DoxR samples.
- Dot plot shows mean expression of key differentially expressed genes in C0 and C5 clusters between control and DoxR samples.
- Monocyte-derived macrophages (MoM) from HCC peripheral blood mononuclear cells (PBMCs) were cultured for 48 hours with conditioned media from patient-derived organoid (PDO) which were either treated with doxorubicin (MoM+ DoxoR PDO CM; n=11,753) or control (MoM+ ctrl PDO CM; n=2089).
- Monocyte-derived macrophages (MoM) from HCC peripheral blood mononuclear cells (PBMCs) were treated with doxorubicin-containing media (MoM+Doxorubicin, n=7559) or doxorubicin-free control media (MoM+ctrl media, n=15,546). Unpaired t-test used to compare the proportion of PDL1+ MoM on flow cytometry.

Abbreviations: HCC- hepatocellular carcinoma; DoxR- Doxorubicin Resistant; PDO- Patient derived organoid; CM- Conditioned media; Ctrl- Control; MoM- Monocyte derived macrophage; PBMCs- Peripheral blood mononuclear cells

Supplementary Figure 11 Spatial transcriptomic analysis of tumor-cell and macrophage areas in HCC

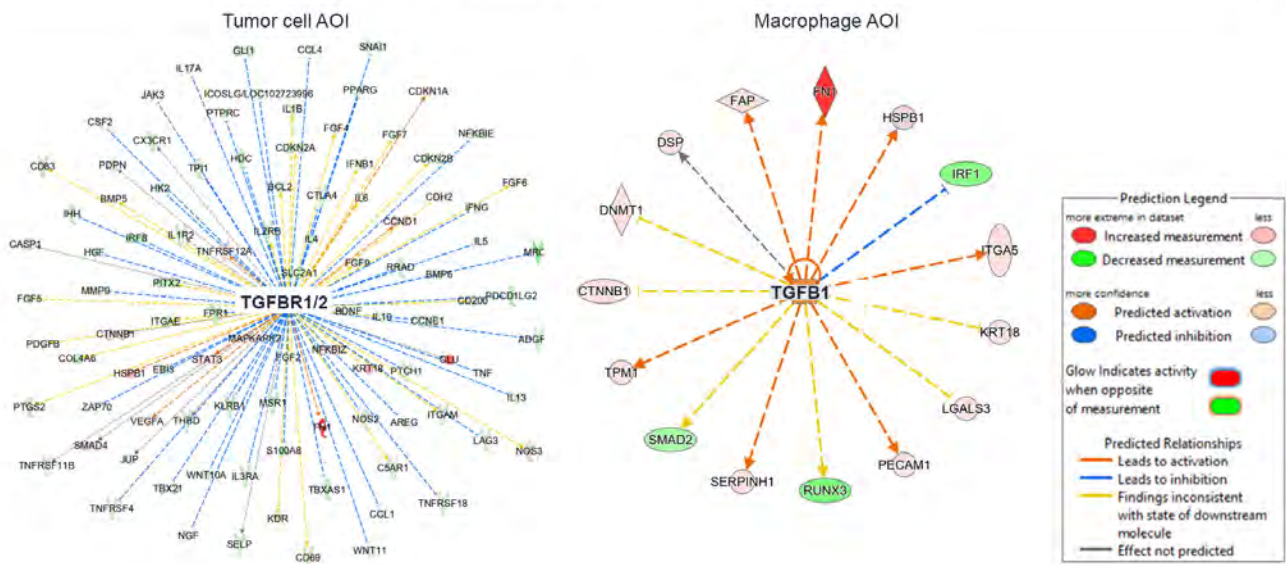
Recurrence-Free Survival

a.



b.

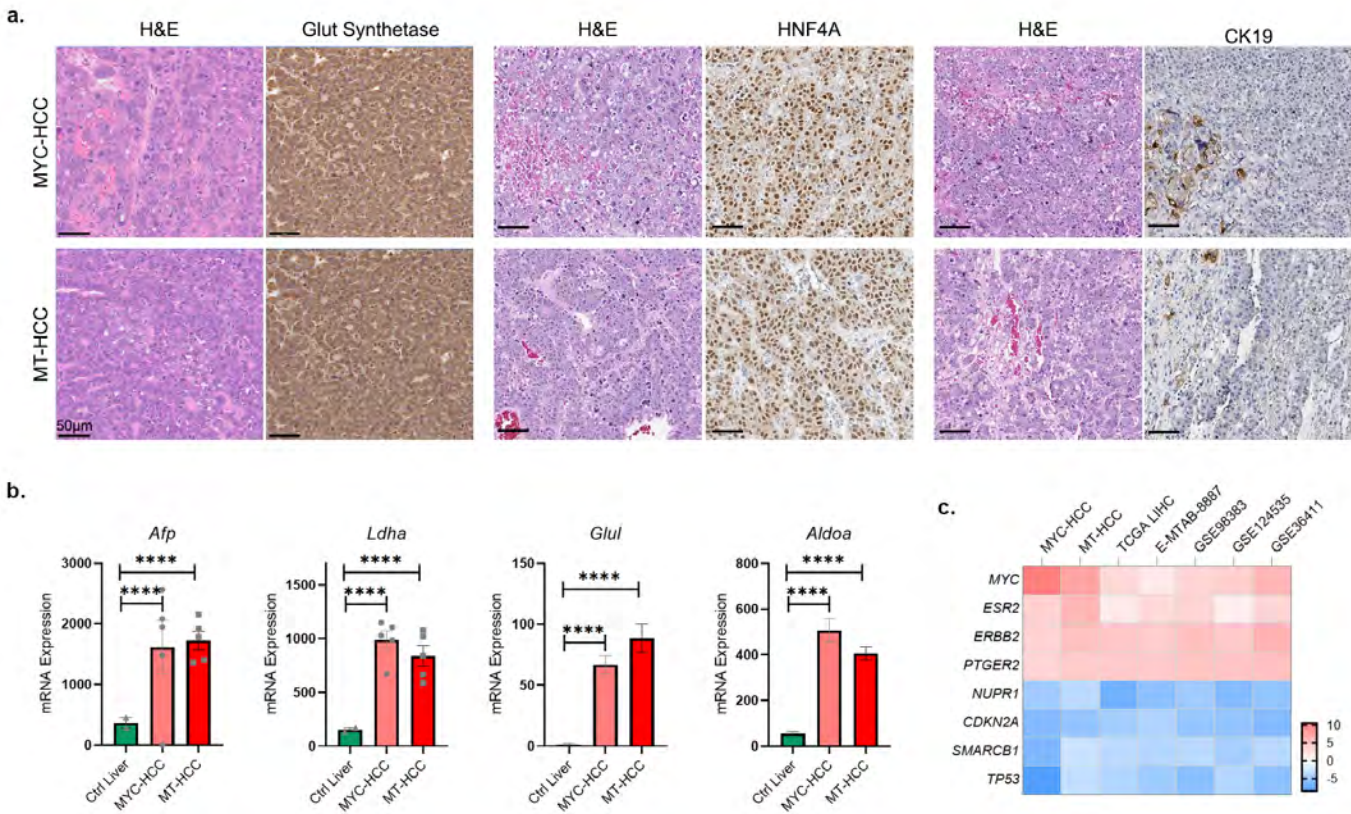
Upstream regulator of transcriptional changes in residual HCC



- Recurrence-free survival predicted by the macrophage and tumor-cell signatures derived from the spatial transcriptomic analysis.
- TGFBR1/2 pathway displayed as an upstream regulator of the network of transcriptional changes in the tumor-cell AOI and the corresponding ligand TGFB1 in the macrophage AOI of residual HCC.

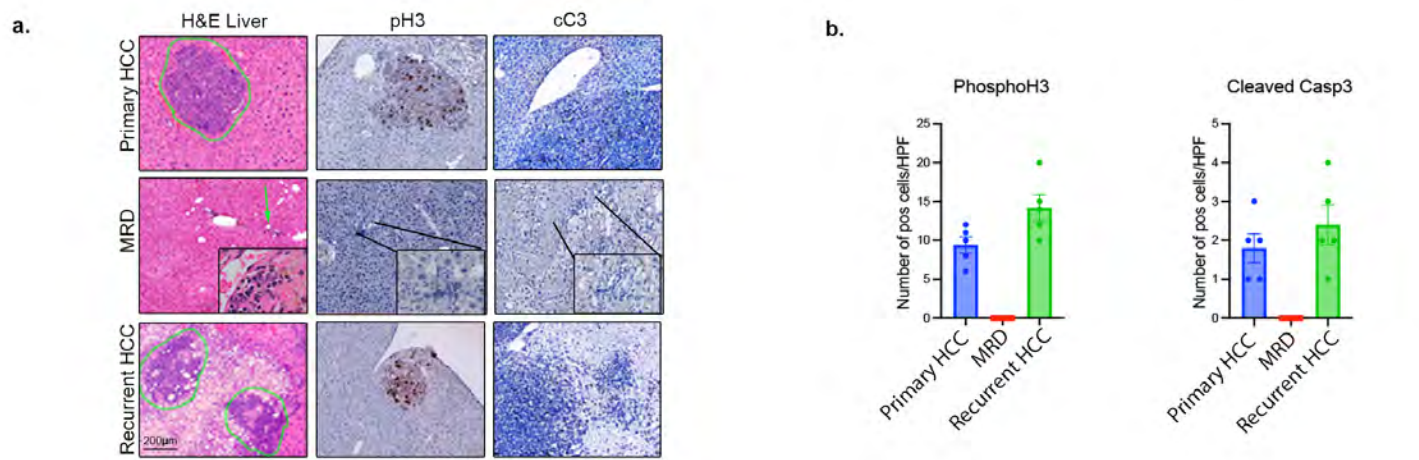
Abbreviations: *TGF* transforming growth factor; *Res-* Residual; *Tum-* Tumor; *HR-* hazard ratio. *AOI-* Area of interest

Supplementary Figure 12 Translational relevance of primary MYC-HCC and MT-HCC



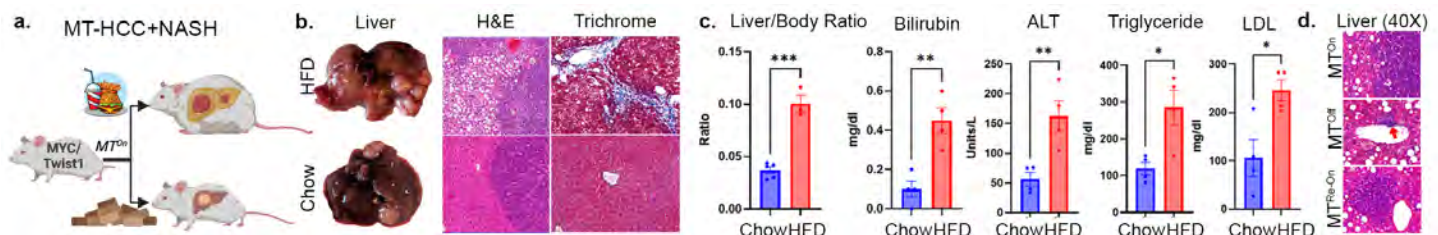
- H&E images and IHC for HCC-specific proteins glutamine synthetase, HNF4A and stem cell marker CK19.
- Expression of HCC-specific genes in primary (MYC-HCC=5, MT-HCC=5) compared to WT FVB mouse liver (n=3). Unpaired t test used to compare the mean between the groups.
- Heat map shows similarity between MYC-HCC=5, MT-HCC=5 and five human HCC transcriptome data sets including the TCGA cohort; the top 5 upregulated and downregulated genes across the different data sets are shown.

Supplementary Figure 13 Dormant tumor cells persist in MRD



- Representative H&E and IHC images showing phospho histone 3 (pH3) and cleaved caspase 3 (cC3) staining in primary HCC, minimal residual disease (MRD), and recurrent HCC in MYC-HCC and MYC-Twist1 HCC livers.
- Bar plots comparing quantification of phospho histone3, and cleaved caspase 3, in primary tumors, MRD, and recurrent tumors in the liver of MYC-HCC ($n=5$) in each group.

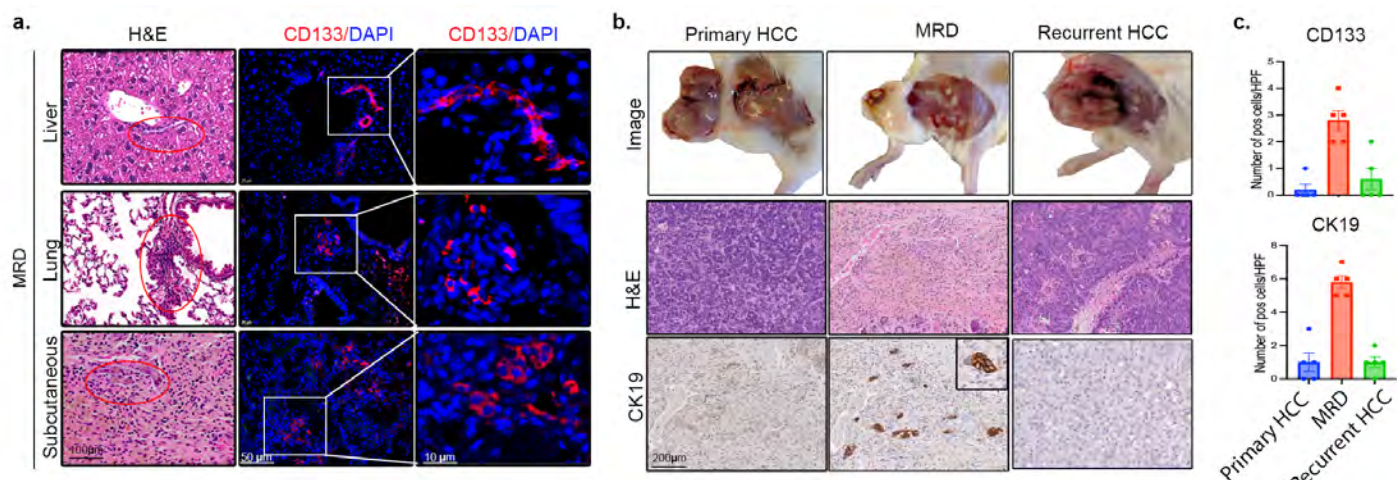
Supplementary Figure 14 Persistence of residual MT-HCC with diet-induced NASH



- Experimental scheme to induce NASH in MT-HCC.
- Gross liver images, H&E, and trichrome staining demonstrating induction of NASH, fibrosis, and HCC in this model.
- Confirming induction of NASH by demonstrating hepatic inflammation, obesity, hyperlipidemia with high fat diet (HFD).
- Confirming reversible residual HCC upon oncogene inactivation in MT-HCC with diet-induced NASH.

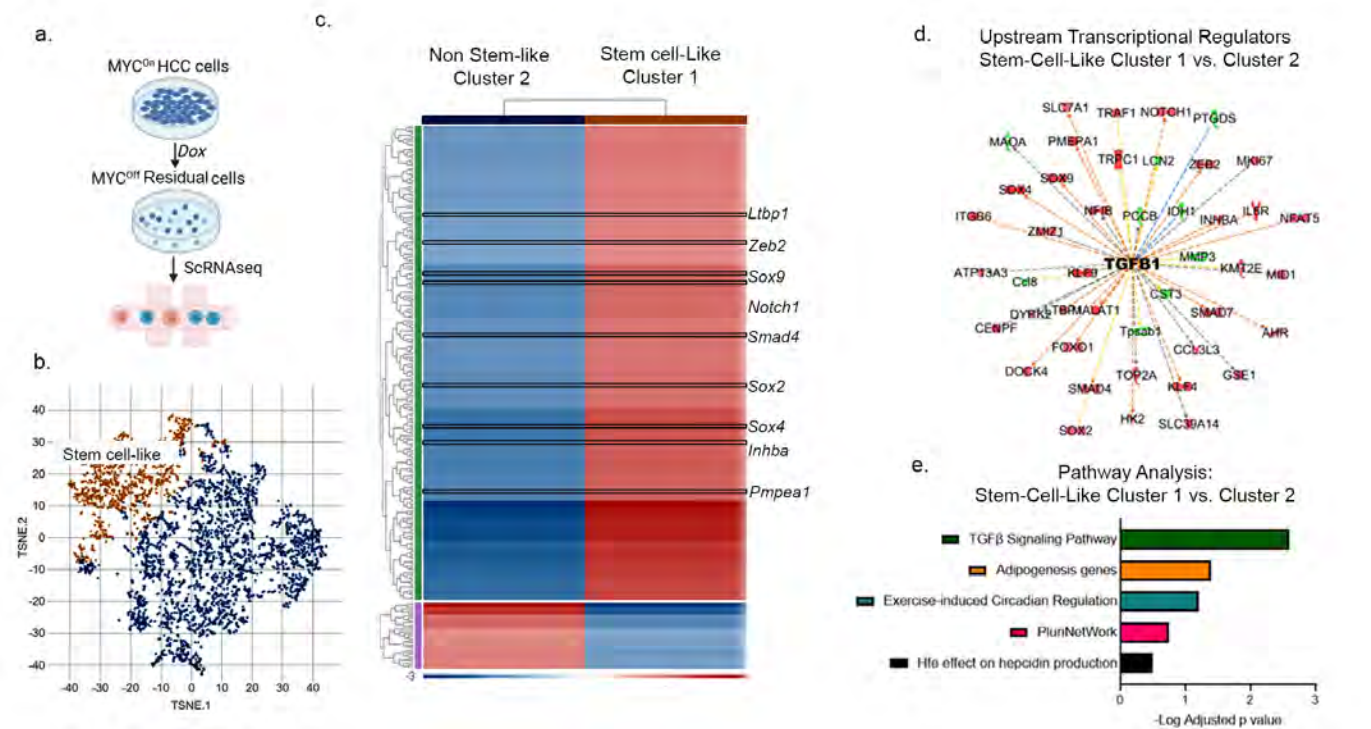
Abbreviations: NASH Nonalcoholic steatohepatitis; MT-HCC MYC/Twist1 HCC; HFD High Fat Diet; ALT-Alanine aminotransferase.

Supplementary Figure 15 Stem-like cancer tumor cells persist in MRD



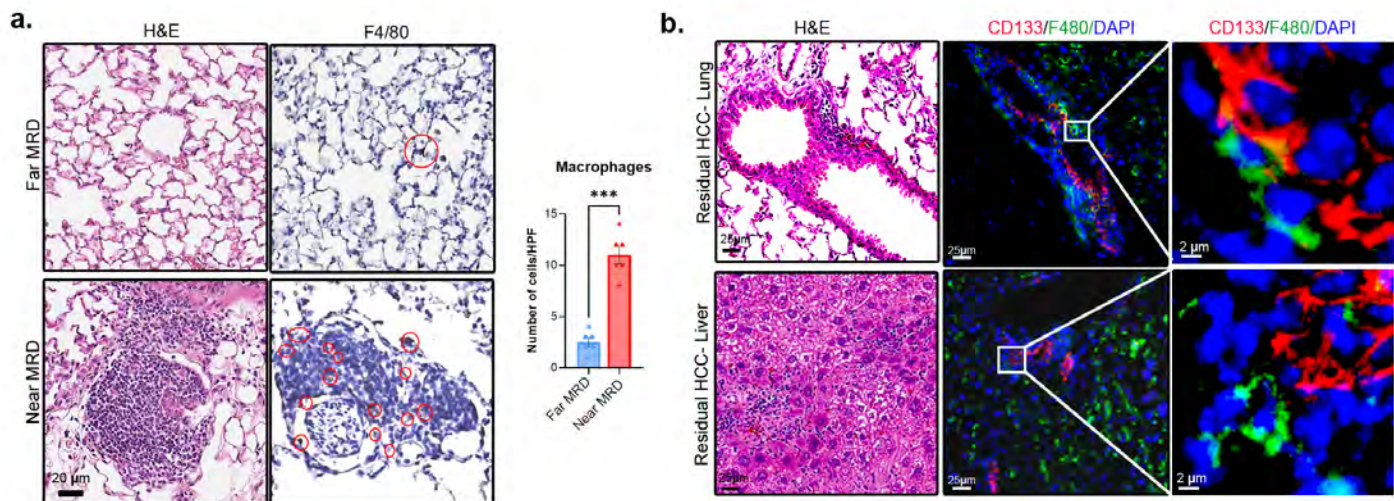
- Representative H&E and IHC images showing persistence of CD133+ stem-like cancer cells in perivascular niches of oncogene inactivated MRD in the liver, lungs and subcutaneous spaces.
- Representative H&E and IHC images showing persistence of CK19+ stem-like cancer cells in perivascular niches of MRD in the subcutaneous spaces.
- Bar plots comparing quantification of CK19 and CD133 in primary tumors, MRD, and recurrent tumors in the liver of MYC-HCC (n=5) in each group.

Supplementary Figure 16 Residual tumor cells demonstrate stemness and activation of Tgf β pathway



- Experimental scheme for single-cell sequencing on MYC inactivation residual tumor cells (n=4367 cells).
- Two major clusters upon MYC inactivation, stem cell-like cluster (n=1184 cells) and non-stem-like cluster (n=3183 cells).
- Heatmap shows differentially expressed genes between the stem cell-like cluster and non-stem-like clusters.
- Activation of Tgf β 1 pathway in the stem cell-like cluster of residual tumor cells.
- Top molecular pathways activated in the stem cell-like cluster.

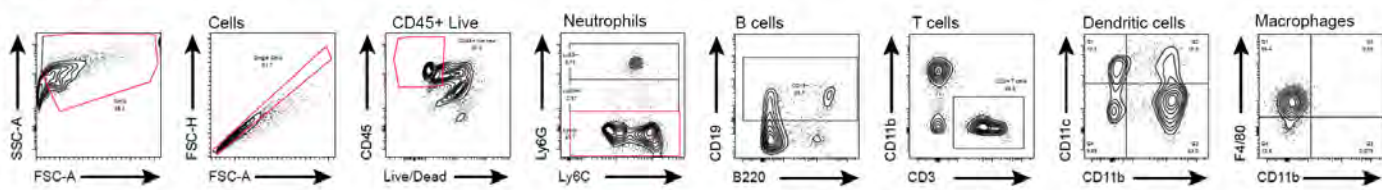
Supplementary Figure 17 Interaction of stem-like cancer cells and macrophages in MRD



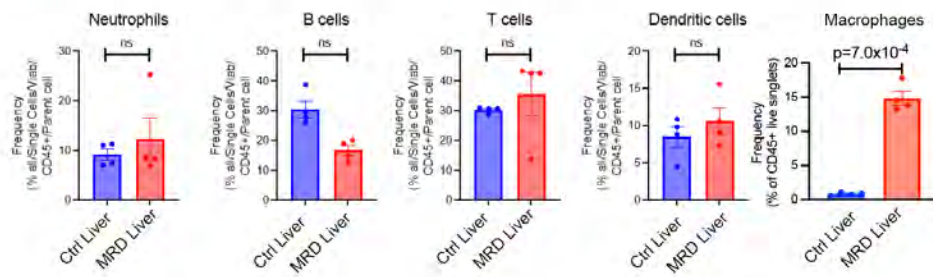
- Comparison of macrophages in the spatial proximity of MRD (n=6) versus areas without MRD (n=6) in the lungs of MYC/Twist1 mice.
- Representative images demonstrating spatial interactions of stem-like cancer cells and macrophages in the spatial proximity of MRD in the lungs and liver of MYC/Twist1 mice.

Supplementary Figure 18 Flow cytometry analysis of in vivo residual HCC niche

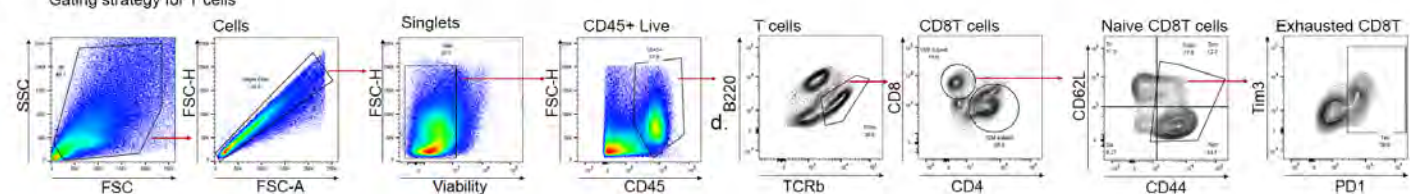
a. Gating strategy for Immune cells



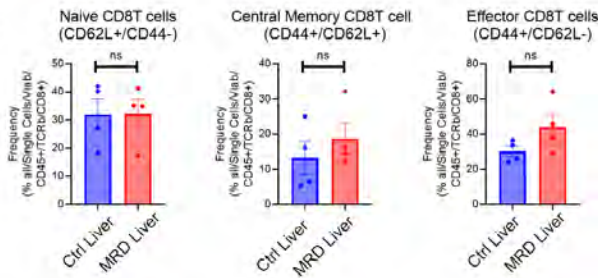
b.



c. Gating strategy for T cells

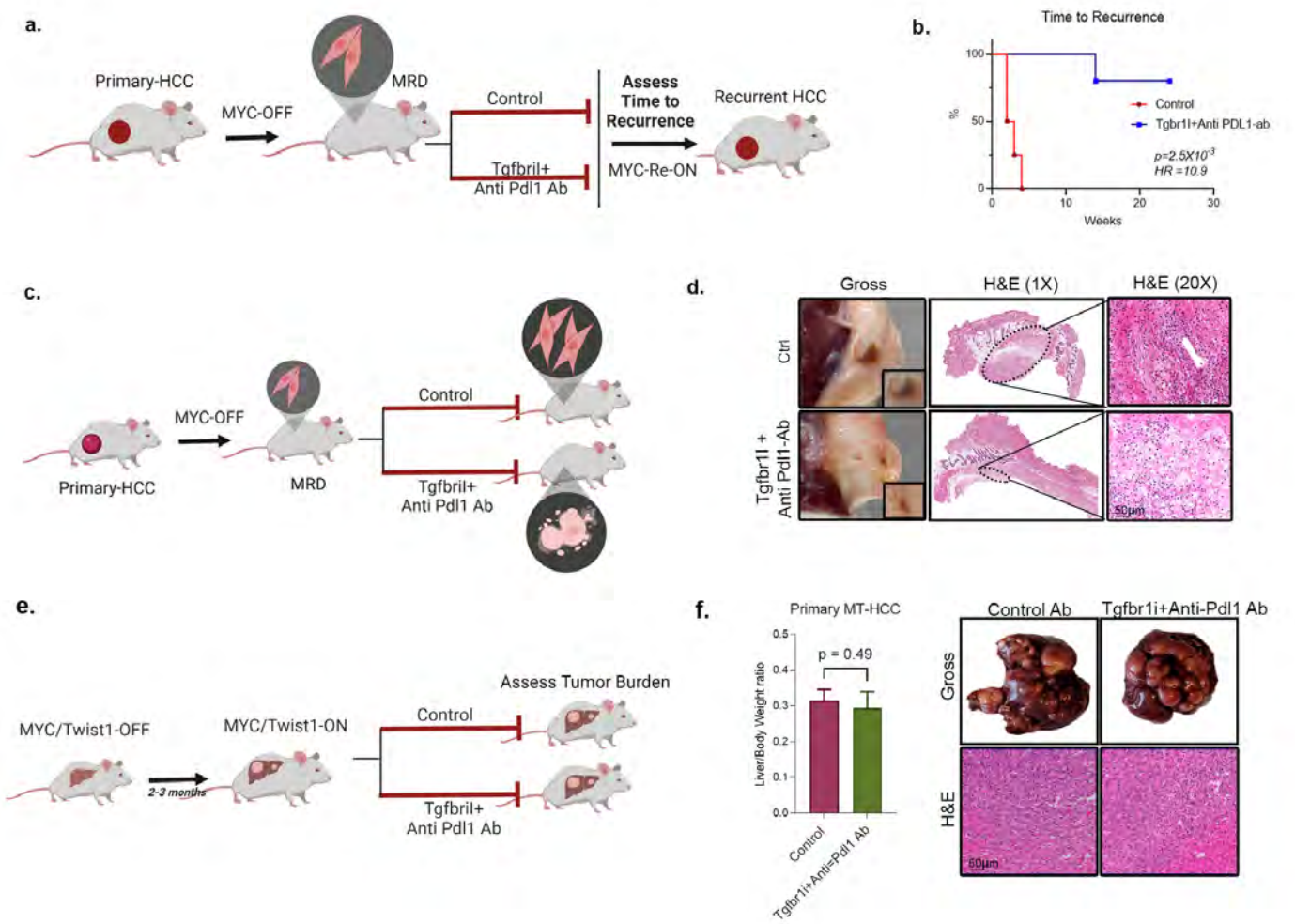


d.



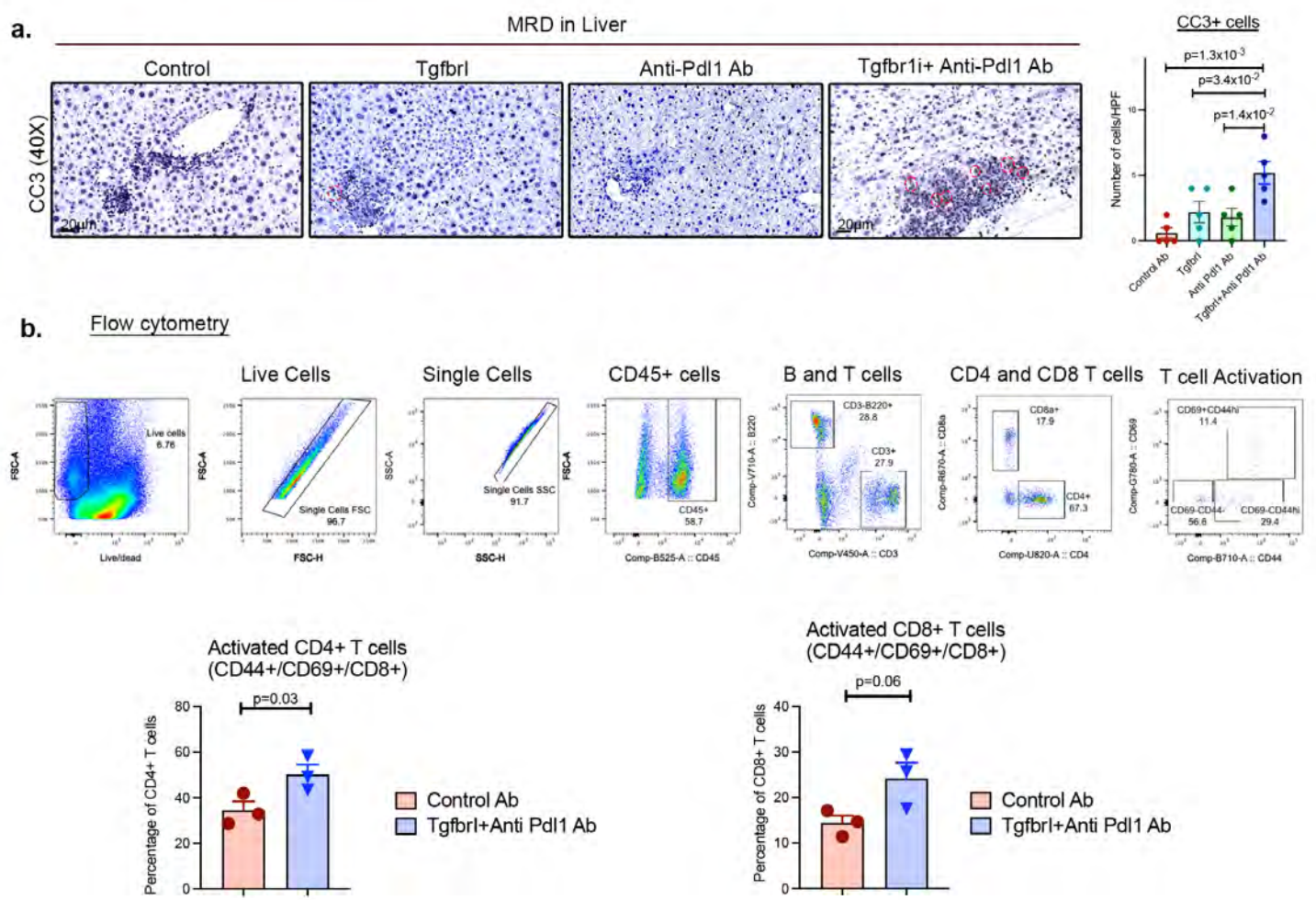
- Flow cytometry gating strategy of innate and adaptive immune cells isolated from livers.
- Comparison of immune cell subsets between livers without MRD ctrl Liver (n=4) and livers with MRD (n=4). Bar plots compared using unpaired t-tests.
- Flow cytometry gating strategy of T cell subpopulation isolated from livers.
- Comparison of CD8T cell subsets between livers without MRD ctrl Liver (n=4) and livers with MRD (n=4). Bar plots compared using unpaired t-tests.

Supplementary Figure 19 Combined blockade of Tgf β r1 and Pdl1 eliminates MRD in subcutaneous allografts but is not effective against primary HCC.



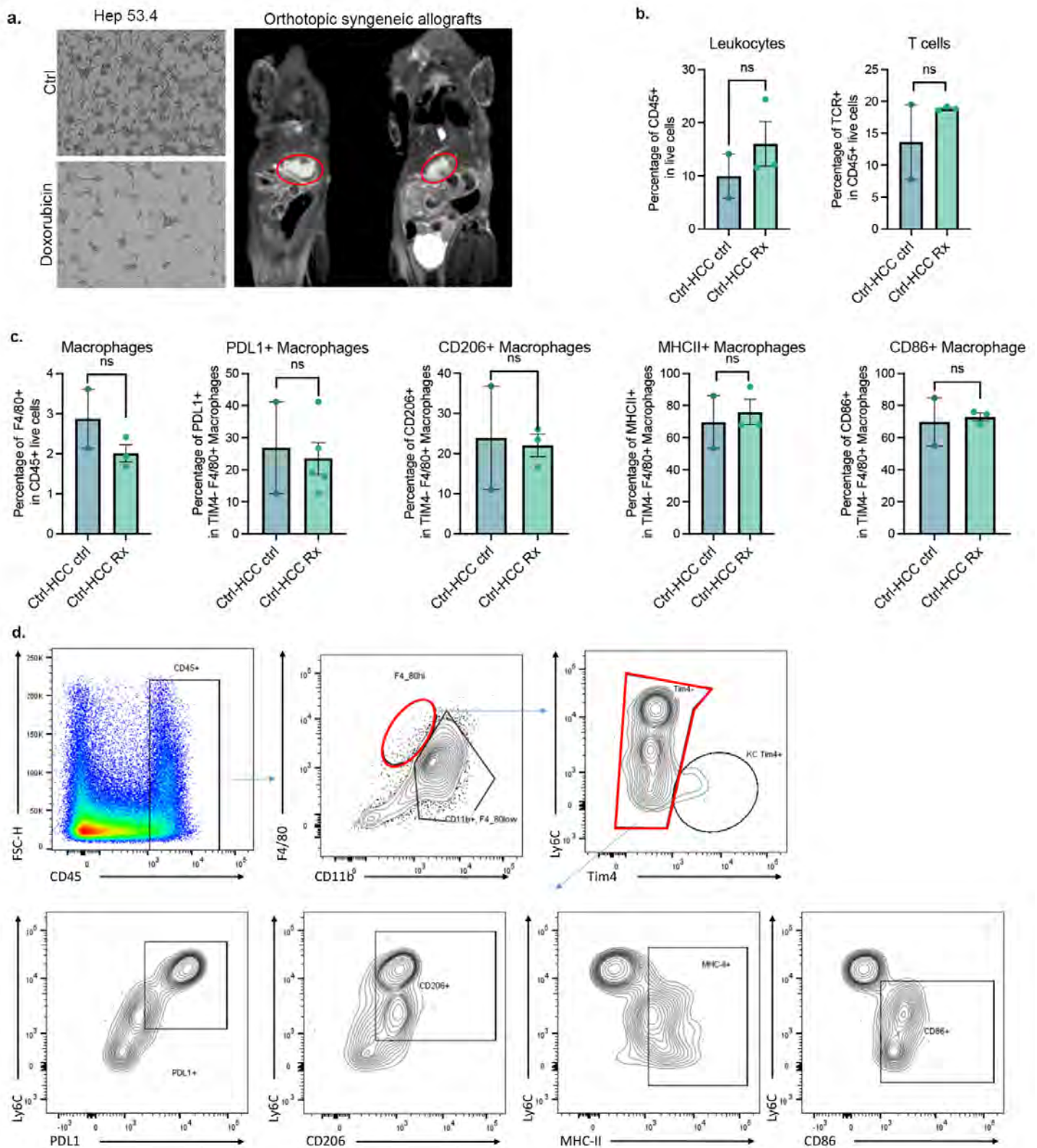
- Experimental scheme for treatment of oncogene-deprived subcutaneous MRD-bearing mice with control antibody or combination therapy with Tgfbr1 and Pdl1 inhibitors. Treatment is followed by oncogene re-activation to induce tumor recurrence.
- Kaplan Meier curves show time to recurrence in oncogene-deprived subcutaneous MRD-bearing mice with control antibody (n=4) or combination therapy with Tgfbr1 and Pdl1 inhibitors (n=5).
- Experimental scheme for treatment of oncogene-deprived subcutaneous MRD-bearing mice with control antibody or combination therapy with Tgfbr1 and anti-Pdl1 inhibitor. Residual tumor niches are then evaluated at the end of treatment.
- Macroscopic and microscopic evaluation of subcutaneous MRD sites shows elimination of residual tumor cells in mice treated with combination therapy with Tgfbr1 and Pdl1 inhibitors (n=4) than control (n=4).
- Experimental scheme for treatment of oncogene-activated primary MT-HCC with control antibody or combination therapy with Tgfbr1 and anti-Pdl1 inhibitor. Liver tumor burden is assessed at the end of treatment.
- Quantification of liver tumor burden, gross images, and H&E images of primary MT-HCC treated with control antibody (n=4) or combination therapy with Tgfbr1 and anti-Pdl1 inhibitor (n=4).

Supplementary Figure 20 Treatment with TGF β and Pd1 inhibitor of residual HCC-bearing mice



- Apoptosis measured by cleaved caspase 3+ cells in liver MRD of MYC-HCC mice treated with control (n=5) versus Tgfbr1 (n=5) or Pd1 inhibitors (n=5) or combination therapy with Tgfbr1 and Pd1 inhibitors (n=5).
- Flow cytometry gating strategy of immune cells isolated from MRD of MYC-HCC mice treated with control versus combined TGF β and Pd1 inhibitors. Flow cytometry quantification of activated CD4 and CD8T cells which are CD69+/CD44^{high} in MRD of mice treated with control antibody (n=3) or combination therapy with Tgfbr1 and Pd1 inhibitors (n=3). Bar plots compare the mean between the groups with unpaired t-tests.

Supplementary Figure 21 Establishing a doxorubicin-resistant syngeneic orthotopic HCC allograft.



- Hep 53.4 HCC cell lines are treated with control or doxorubicin for 96 hours and viable cells are selected for orthotopic implantation into mouse liver, confirmed by MRI.
- Flow cytometry analysis shows no difference in leukocyte or T cell infiltration in WT mice bearing control HCC treated with either control antibody (n=2) or combined inhibition of Tgfb1 and anti-Pd1 antibody (n=3). Bar plots compare the mean between the groups with unpaired t-tests.

- c. Flow cytometry analysis shows no difference in macrophage subsets in WT mice bearing control HCC treated with either control antibody (n=2) or combined inhibition of Tgfb1 and anti-Pdl1 antibody (n=3). Bar plots compare the mean between the groups with unpaired t-tests.
- d. Flow cytometry gating strategy of macrophages isolated from orthotopic syngeneic allograft-bearing mice.